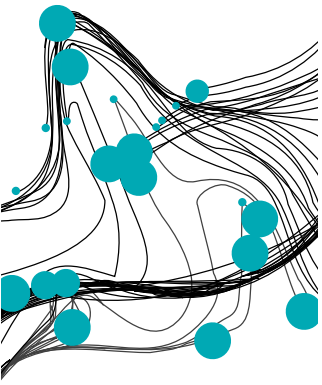

RAM ROBOTICS AND MECHATRONICS

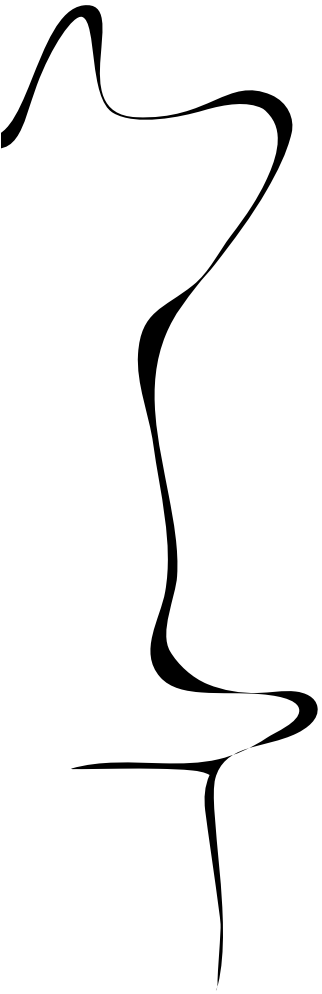

3D PRINTED ELECTRICALLY CONTROLLED PNEUMATIC VALVE

H.S.V.C. (Hemanth) Jaladi

MSC ASSIGNMENT

Committee:
prof. dr. ir. G.J.M. Krijnen
ir. M. Schouten
dr. ir. D. Alveringh

May, 2021

026RaM2021
Robotics and Mechatronics
EEMathCS
University of Twente
P.O. Box 217
7500 AE Enschede
The Netherlands

UNIVERSITY OF TWENTE. | TECHMED CENTRE UNIVERSITY OF TWENTE. | DIGITAL SOCIETY INSTITUTE

Summary

Pneumatic switches work essentially like valves that can control the flow of air. The context for this assignment is to use electrically controlled thermal actuation to direct the flow of air for switching pressure which can be used to guide the insertion tube on an endoscope. To accomplish this, a flexible membrane that expands with the thermal expansion of the liquid within the actuator and contracts while cooling is used to switch the flow. To understand the process of heat flow within the actuator, the heat flow in a 1-D infinitely long plate and a sphere while cooling and also a sphere with uniform heat source are studied. For this study both an analytical model as well as an FEM model are used. Finally a 3D printed design is made to study the functioning of the heater and the temperature distribution inside the actuator in practice. Using thermocouple measurement and IR thermography, spatio-temporal temperature distributions of the 3D printed actuator are obtained and compared with the results of the models.

Contents

List of Figures

List of Tables

1 Introduction

This work describes the work done by Hemanth Jaladi for his final master assignment. The report is about 3D printing of an electrically controlled pneumatic switch. The assignment is to design an 3D printed thermal actuator for the purpose of switching the airflow into an endoscope insertion tube chamber. [2]

1.1 Related work

Pneumatic actuators are used in a wide range of applications in different industries like soft-robotics and process engineering. Pneumatic systems are well-known for their simplicity, low cost, ease of maintenance, and safety [3]. There are different types of pneumatic actuators which use various actuation and control techniques. An electro-pneumatic valve using solenoid operated with pulse width modulation (PWM) control is used in [4] for fast switching. In [5] a control strategy using acceleration feedback is implemented to improve the stability of servo-pneumatic actuators. In McKibbens flexible artificial muscles, an inner elastic tube and braid is used [6]. As a muscle is pressurised, its thickness expands, i.e. its diameter expands while its length contracts [7]. In [6] a silicon tube and springs are used to realise a flexible actuator with high elongation than can be used in pneumatically driven robotic devices. In case of typical hydraulic actuators, a pressurised liquid with the use of servo motors and pistons are used to induce the required stroke [8] [9]. In [10] and [11] a thermo-pneumatic actuation principle is used in application of MEMS devices. In [12] multi-material additive manufacturing is used to design a soft thermal actuator using a PLA and paper bilayer composite for electrical switching and a numerical model is used to predict the transient behaviour. In [13] a phase change actuator, which uses volume expansion due to change in phase of the fluid from liquid to gas, is built using an inkjet printed conductive flexible circuit. In [14], for the purpose of solar tracking, a thermal hydraulic actuator is built using methyl-alcohol as working fluid and solar heating is used for thermal actuation [15] [16].

In this assignment the design of a thermal-hydraulic actuator for pneumatic switching, based on thermal expansion of liquid to induce bidirectional actuation, and using a flexible membrane that can be fabricated through FDM (Fused deposition modelling), is investigated. For an actuator a final decision on the appropriate type and design configuration be made only in relation to the needs of a specific application. So the actuator is designed for the use of pneumatic switching in endoscopy insertion tube chambers mentioned in [2].

1.2 Project Goals

The goal of the project is to design and 3D print a thermal actuator which can be electrically controlled for the purpose a pneumatic switch that can be used to switch the pneumatic supply lines of an endoscope.

1.3 Research questions

To attain the presented goal, it will be broken down into specific research questions

- Which analytical (mathematical) equations have a close relation to heat flow in a thermal actuator?
- What are the materials that can be used to 3D print an electro-thermal actuator using FDM printing? Can these materials be helpful in attaining the required actuator specification?
- What are the electrical and thermal properties of a 3D printed heater?

- What are the design requirements for the actuator to attain a switching time of 1.5 s and block a tube of diameter 2 mm?

1.4 Approach

To approach the goal, initially an analytical model is constructed to study the feasibility to help us design the final actuator. To support this analytical model a similar FEM model is built. The simulation results of the analytical model and the FEM model are compared and a time constant is attained from both models. Next, various design approaches are discussed and a test structure which can help in studying the working of the actuator is designed and later 3D printed using FDM. Afterwards, experiments are performed on this test structure using a thermal camera and a thermocouple. Finally, these measurements are analysed and the time constants are determined for the test structures with varying supplied powers. To see how much power is needed to reach the required temperature change to check if the time constants vary significantly for high temperatures.

1.5 Report structure

First in chapter 2, the analytical models for simple geometries like 1D slabs and spheres with various steady state and transient situations are studied and cross-referenced with FEM models. In chapter 3, different concepts for actuator design are discussed and the material properties and their feasibility for 3D printing of the actuator are investigated. Finally an actuator structure is designed for testing the temperature distribution inside the actuator. In chapter 4, fabrication of the designed test structure from chapter 3 using FDM 3D-printing is discussed and various print settings used in fabrication are presented. In chapter 5, various measurements performed on the actuator model and how the measurements are performed are presented. In chapter 6, the results obtained from the experiments mentioned in chapter 5 are presented. Finally in chapter 7, the overall discussion and conclusions are presented.

2 Model

In this chapter, various analytical studies are conducted to study heat transfer in simple geometries like a slab (or plane wall) and a sphere. Furthermore, these studies are performed in both steady-state and transient situations with particular defined boundary conditions that can be used to solve for a solution.

Initially, a steady-state condition for a slab and a sphere (without heat generation) is considered, and analytical equations for determining the temperature at a certain point in these geometries are obtained. Later, transient analysis is performed for the same geometries. In the transient analysis, a situation termed quenching (forced cooling) is considered for both a slab and a sphere and the analytical solutions are determined. Furthermore, to closely represent an experimental situation, a transient situation with internal heating and convective boundaries is analyzed and the analytical solution is determined. These studies are done with a compromise between the mathematical complexity and the relevance to the case study of the physical model.

The obtained transient analytical equations are used to implement MATLAB simulations. Moreover, Finite Element Model models are built in ComSol according to the analyzed transient situations and the obtained simulations are then compared to the respective MATLAB simulations.

2.1 Analytical model

Since the concept behind the actuator is to use thermal actuation, it is essential to perform an approximate study of heat conduction in various models before designing the actuator. This will be helpful in identifying the process of heat conduction and the calculation of heat generation requirements. For this purpose, analytical solutions for simple geometries are studied. Analytical solutions give a better understanding of how different parameters effect the temperature distribution. Furthermore, these results can be extended to the experimental model, offering approximate requirements on design parameters in designing the actuator in real-time. Since ideal conditions are assumed in the analytical analysis in order to simplify complex problems, there will be some inconsistencies between the analytical model and the actual physical model.

Heat flow or heat conduction analyses are often categorised as steady-state and unsteady-state (or transient) [17, P. 63]. In a steady-state, the temperature of the model is considered to not vary with time i.e., the temperature distribution is dependent only on the position. In an unsteady state or transient situation, the temperature changes with both time and position.

This section is limited to a 1-dimensional study i.e., the heat transfer in the model is considered along one direction and is considered negligible in the other directions. To analytically model the heat conduction in a step-by-step process and to simplify the mathematical equations involved, first the models are solved for simple geometries like a slab and a sphere in 1D steady-state and later extended to 1D transient cases. Finally, the transient solution is obtained for a spherical model with internal heat generation and convective boundaries. Various mathematical approaches exist like nondimensionalization, separation of variables [18, P. 248-251] [19] [20, P. 75-221], energy balancing [17, P. 275] and Heisler charts [17, P. 218-222] to perform heat flow analysis. In this report, separation of variables is used to solve the equations in different cases of heat conduction in transient analysis of slab and sphere.

In solving the differential equations, it is important to select the boundary conditions to closely represent the physical conditions, as boundary conditions play a critical role in analytical solution and its representation [20, P. 75]. For deriving these analytical solutions, proper coordinate systems should be used depending on the model. For a slab and a sphere, a Cartesian

coordinate system and a spherical coordinate system are used respectively. The use of these coordinate systems simplifies the solution of these problems. [21]

MATLAB simulations are done by discretizing the analytical solutions. The results of the MATLAB simulations are verified by COMSOL simulations by building the model in close approximation to the analytical solution's assumptions.

Transient Case(s)	**Boundary Condition(s)**	**Initial Condition(s)**
Slab With Imposed Boundary	$U(0,t)=0$ and $U(L,t)=0$	$U(x,0)=f(x)$
Sphere with Imposed Boundary	$\frac{\partial U}{\partial r_{r=b}}=0$ and $U_{r=b}=0$	$U_{t=0}=f(r)$
Sphere with Internal heat generation	$U(r\to 0) \implies$ finite and $-k\frac{\partial U}{\partial r_{r=b}}=hU$	$U_{t=0}=f(r)$

Table 2.1: Initial and boundary conditions for slabs and spheres with quenching, and spheres with internal heat generation

2.2 Slab

2.2.1 Slab in 3 Dimension

The partial differential equation representing the heat conduction in a 3D slab (in Cartesian coordinates) is given by [17, P 74-75]:

$$\frac{\partial^2 U}{\partial x^2}+\frac{\partial^2 U}{\partial y^2}+\frac{\partial^2 U}{\partial z^2}=\frac{1}{\alpha}\frac{\partial U}{\partial t} \tag{2.1}$$

Where,

- x, y, z represents position along each axis
- t is time.
- U is the temperature in the model or medium with respect to position and time. Also represented as $U(x,y,z,t)$.
- α is the thermal diffusivity of the material and equals $\frac{k}{\rho c}$ with k the thermal conductivity, ρ the mass-density and c specific heat.

2.2.2 Steady State Analysis

The figure 2.1 represents a slab or plain wall with thickness L. The temperatures at the boundaries $x=0$ and $x=L$ are T_1 and T_2 respectively.

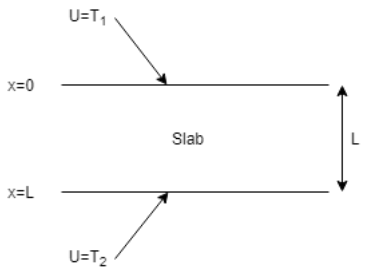

Figure 2.1: Slab in steady state with initial and boundary conditions

In steady state analysis, at any time the temperature along the slab is considered constant. The thermal heat distribution of the slab can be effectively solved using a 1D analysis. In case of one dimensional heat flow, considering the change in heat flow is only along the x-direction,

the equation(2.1) becomes [22]

$$\frac{\partial^2 U}{\partial x^2} = \frac{1}{\alpha}\frac{\partial U}{\partial t} \tag{2.2}$$

In steady state analysis there is no change in temperature with respect to time. Therefore, U is only a function of position, the equation 2.2 becomes

$$\frac{\partial^2 U}{\partial x^2} = 0 \tag{2.3}$$

By integrating equation 2.3 the following equation is obtained

$$U = ax + b \tag{2.4}$$

To determine U, a and b need to be determined which are obtained by using the boundary conditions as shown in fig 2.1. Applying the boundary conditions $U(0) = T_1$ and $U(L) = T_2$ to 2.4 gives [17, P. 88]

$$U = T_1 + \frac{T_2 - T_1}{L}x \tag{2.5}$$

The equation (2.5) determines the temperature U within the slab at any given position x.

2.2.3 1D Transient Analysis of Slab

As mentioned the transient analysis is done in one dimension, because it is relatively easy to study. To solve the 1D transient problem, it is required to define both initial conditions as well as boundary conditions, representing the particular scenario or case that the solution obtained is applicable for. One such case is the imposed boundary representing a quenching problem.

Slab with quenching Boundary Conditions

In this section a slab, as shown in fig 2.2, is considered to be in a transient state, the temperature within the slab changes with both position and time.

Figure 2.2: Slab Quenching with boundary conditions

For transient analysis, the problem of quenching is considered which implies that boundary conditions are used in which the (relative) temperature at boundaries is zero at any given position and time

The analysis starts by rewriting Equation 2.2 as: [19] [23] [24, P. 48]

$$\frac{\partial U}{\partial t} = \alpha\frac{\partial^2 U}{\partial x^2} \tag{2.6}$$

The analysis will use the following initial and boundary conditions

$$\begin{aligned} U(0,t) &= 0 \\ U(L,t) &= 0 \\ U(x,0) &= f(x) \end{aligned} \tag{2.7}$$

Where $U(x,t)$ is the temperature at position x at time t. $U(x,0) = f(x)$ is the initial condition. To solve the differential equation, separation of variables will be used. [18, P. 248]

$$U(x,t) = X(x)T(t) \tag{2.8}$$

Substitution of equation 2.8 into equation 2.6 results in

$$X\frac{\mathrm{d}T}{\mathrm{d}t} = \alpha T\frac{\mathrm{d}^2X}{\mathrm{d}x^2} \tag{2.9}$$

Using the definitions $\dot{T} = \frac{\mathrm{d}T}{\mathrm{d}t}$ and $X'' = \frac{\mathrm{d}^2X}{\mathrm{d}x^2}$ this equation can be rewritten as

$$X\dot{T} = \alpha T X'' \tag{2.10}$$

Dividing on both sides by $X(x)T(t)$ gives

$$\frac{\dot{T}}{T} = \alpha\frac{X''}{X} \tag{2.11}$$

Since this has to be true for all values of x and t and since the lhs only depends on t and the rhs only on x, the only possibility is that both sides are one and the same constant'λ':

$$\begin{aligned}\frac{X''}{X} &= \lambda \\ \frac{\dot{T}}{T} &= \alpha\lambda\end{aligned} \tag{2.12}$$

where $\lambda = \nu^2$. Solving the above equations using boundary conditions, we have three possibilities $\lambda < 0, \lambda = 0$ and $\lambda > 0$. For $\lambda > 0$ and $\lambda = 0$ the solutions are trivial [23, P. 6]. When λ<0, the general solution for $\frac{1}{X}\frac{\mathrm{d}^2X}{\mathrm{d}x^2} = -\nu^2$ is

$$X(x) = A\cos(\nu x) + B\sin(\nu x) \tag{2.13}$$

This only results in a stable and therefore realistic solution if

$$\lambda = -\nu^2 < 0 \tag{2.14}$$

After applying the boundary conditions in 2.7 it is found that

$$\begin{aligned}A &= 0 \\ B\sin\nu L &= 0\end{aligned} \tag{2.15}$$

The only possible solution which solves the boundary condition at $x = L$ is $\nu L = n\pi$. [23, P. 6] This implies $\nu = n\pi/L$. Therefore, the solution satisfying the boundary conditions is

$$X(x) = B\sin\left(\frac{n\pi}{L}\right) \qquad \text{for} \quad n = 1,2,3,... \tag{2.16}$$

Now solving Equation 2.12 for T(t)

$$\dot{T} = -\nu^2\alpha T(t) \tag{2.17}$$

Results in the following solution

$$T(t) = Ce^{-\alpha\nu^2 t} \tag{2.18}$$

Which after substituting $\nu = \frac{n\pi}{L}$ becomes

$$T(t) = Ce^{-\alpha\frac{n^2\pi^2}{L^2}t} \tag{2.19}$$

Substitution of equation 2.19 and 2.16 in 2.8

$$U(x,t) = B\sin\left(\frac{n\pi}{L}x\right)Ce^{-\alpha\frac{n^2\pi^2}{L^2}t} \tag{2.20}$$

Above equation is true for any integer value of n

$$U(x,t) = \sum_{n=1}^{\infty} B_n \sin\Big(\frac{n\pi}{L}x\Big) C e^{-\alpha \frac{n^2\pi^2}{L^2} t} \tag{2.21}$$

In order to obtain the coefficients B_n the initial temperature profile $U(x,0) = f(x)$ will be used.

$$f(x) = U(x,0) = \sum_{n=1}^{\infty} B_n \sin\Big(\frac{n\pi}{L}x\Big) \tag{2.22}$$

Multiplying both sides by the term $\sin\big(\frac{m\pi}{L}x\big)$, integrating over the whole length of the slab and using orthonormality of the sine functions

$$\int_0^L f(x) \sin\Big(\frac{m\pi}{L}x\Big)\,dx = \int_0^L \sum_{n=1}^{\infty} B_n \sin\Big(\frac{n\pi}{L}x\Big) \sin\Big(\frac{m\pi}{L}x\Big)\,dx \tag{2.23}$$

Since B_n is a constant, the right hand side can be written as,

$$\int_0^L f(x) \sin\Big(\frac{m\pi}{L}x\Big)dx = \sum_{n=1}^{\infty} B_n \int_0^L \sin\Big(\frac{n\pi}{L}x\Big) \sin\Big(\frac{m\pi}{L}x\Big)\,dx \tag{2.24}$$

The solution of the integral $\int_0^L \sin\big(\frac{n\pi}{L}x\big) \sin\big(\frac{m\pi}{L}x\big)\,dx$ is,

$$\begin{cases} \frac{L}{2} \text{ if } m = n \\ 0 \text{ if } n \neq m \end{cases} \tag{2.25}$$

Rewriting Equation 2.24,

$$\int_0^L f(x) \sin\Big(\frac{m\pi}{L}x\Big)dx = \sum_{n=1}^{\infty} B_n \frac{L}{2} \delta_{mn} \tag{2.26}$$

where δ_{mn} is defined to be one in case $m = n$ and zero otherwise. From equation (2.23) the solution of B_n is obtained for $n = m$ is [23, P.]

$$B_n = \frac{2}{L} \int_0^L f(x) \sin\Big(\frac{m\pi x}{L}\Big) \tag{2.27}$$

This equation can be used to obtain the final temperature distribution.

$$U(x,t) = \sum_{n=1}^{\infty} B_n \sin\Big(\frac{n\pi}{L}x\Big) e^{-\alpha \frac{n^2\pi^2}{L^2} t} \tag{2.28}$$

where $f(x)$ represents the initial condition of the slab. $U(x,t)$ represents the temperature at a point x at a time t.

Matlab results

A MATLAB model is implemented to simulate the heat distribution in a slab with quenching boundary conditions, by taking the solutions from the above analytical solution. B_n is calculated for n =1 to 1000 using equation (2.27) based on the actual physical parameters of olive oil [25]. The values of these parameters are shown in table 2.2.
The graph 2.3 represents the temperature profile in a slab for the quenching boundary problem represented by equation 2.28. The time required for a 0.02 m long slab to reach steady state is observed. Since, the study is for imposed boundary conditions, where the temperature assumed at boundaries is always 0 °C, and since there is no heat generation, it can be expected that the time needed for the total thickness of the slab to reach 0 °C is the time required to reach steady state. However, using the Equation 2.28 the temperature reaches a near 0 °C but not 0 °C.

Therefore, the time constant for the system is determined. The time required for a 0.02 m long slab at 60 °C elevated temperature to reach 22 °C elevated temperature (which is 1/e times of the initial elevated temperature) at the centre of slab is approximately 551.36 s, which is the time constant of the considered model. The time constant is shown in Figure 2.5, where the temperature vs time is plotted at the centre of the slab and 'Tc' in the figure denotes time constant. The temperature is studied in °C scale. As the boundary conditions are taken on the °C scale.

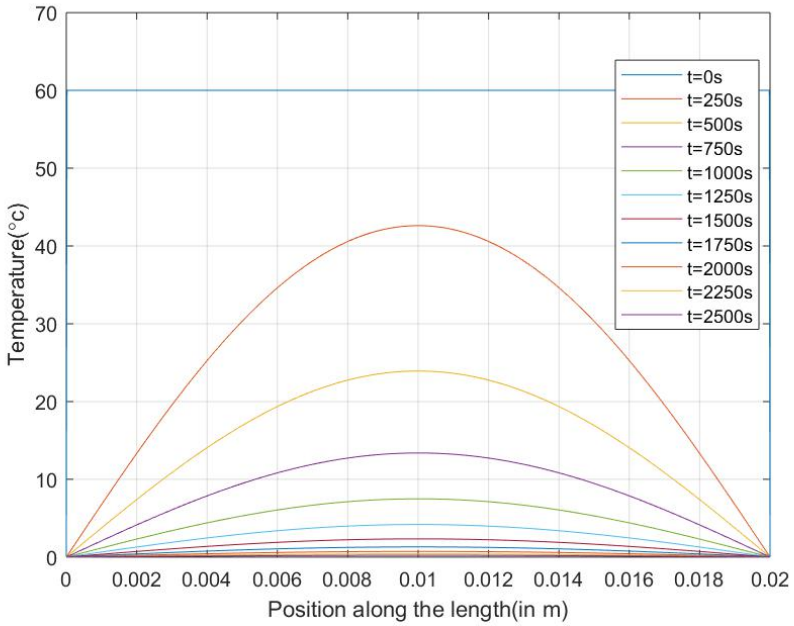

Figure 2.3: Temperature profile from MATLAB simulation of transient quenching analysis of a slab, n =1000.

Parameters/Settings	**MATLAB**	**COMSOL**
Length of slab (L) (m)	0.02	0.02
Initial temperature with in slab	60 °C	333.15 K
Set temperature at boundaries	0 °C	273.15 K
Thermal conductivity k ($\mathrm{W\,m^{-1}\,K^{-1}}$)	0.17	0.17
Density ρ ($\mathrm{kg\,m^{-3}}$)	917	917
Heat capacity c ($\mathrm{J\,kg^{-1}\,K^{-1}}$)	1970	1970
Thermal diffusivity α ($\mathrm{m^2/s}$)	9.4105×10^{-8}	9.4105×10^{-8}
Simulation end time (s)	2500	2500
Cross-section Area	Not required	$1\,\mathrm{m^2}$
n terms	1000	Not required

Table 2.2: Slab with Imposed boundary: Settings on MATLAB and COMSOL.

COMSOL heat flow simulation

The physical parameters that were used in the MATLAB simulation were also used to build a FEM model. By using the Heat transfer module in Solid physics the results are obtained through time-dependent study analysed for a time period of 2500 s and graphs are plotted for every 250 s to observe the heat flow at different times as shown in Figure 2.4. The time constant(time required to reach 1/e of the initial temperature) from the attained graph is 557.24 s, shown in

Figure 2.5. In COMSOL, the temperature input is given in Kelvin scale, but the end graphs are presented in °C.

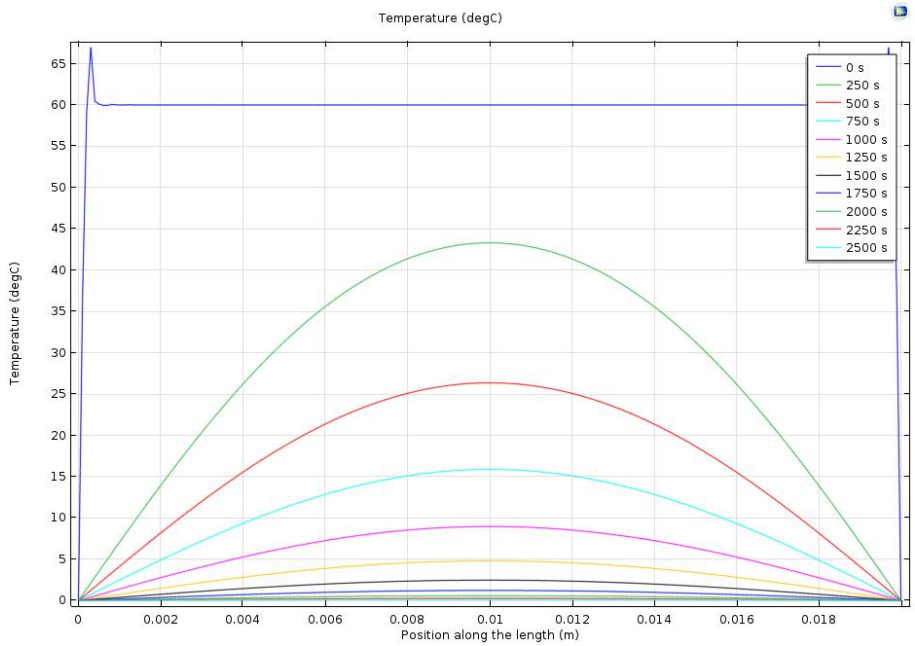

Figure 2.4: Temperature profile from COMSOL simulation of transient quenching analysis of slab

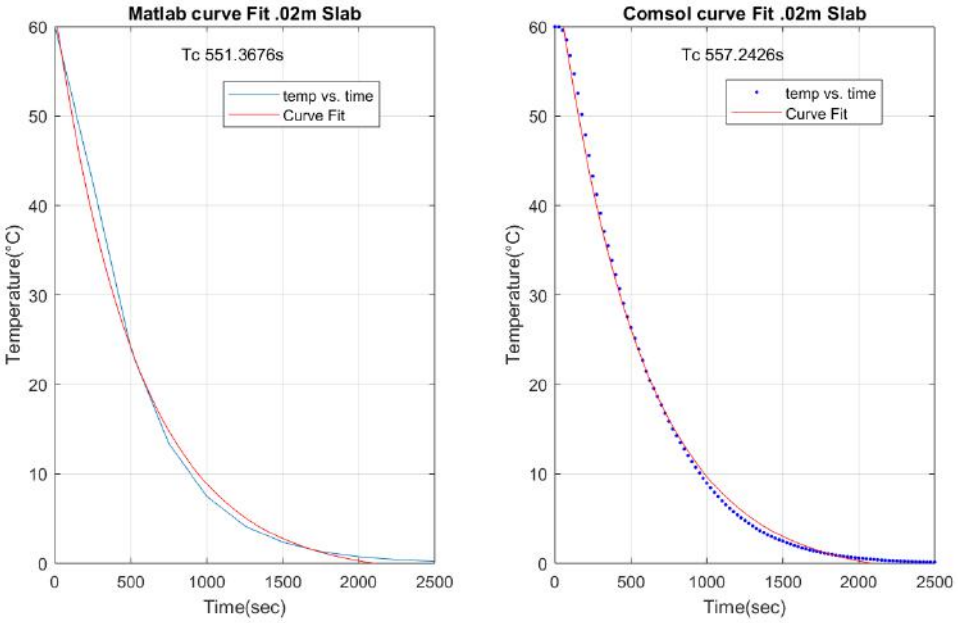

Figure 2.5: Time constant (τ) when temperature at the centre of the slab is plotted, in MATLAB (left side) and COMSOL (right side) by curve fitting. Same time points are taken for curve fitting as shown in Figure 2.3 and Figure 2.4

2.2.4 Conclusion slab analyses

The results of the analytical equations, as used in MATLAB, and the COMSOL model simulations are shown in figures 2.3 and 2.4 respectively. It can be discerned that there is a similar trend in temperature change with position and time. The temperatures used in the analysis

represent the relative temperature difference. These simulations are further compared in terms of time constant(τ) when the centre point of the slab is selected and temperature vs time graph is potted as shown in Figure 2.5. The 'Tc' in the figure is the time constant of the exponential curve fit and there is an error of 1 % in time constant between the MATLAB and COMSOL model. Since both the models show a similar behaviour, it is concluded that they are consistent.

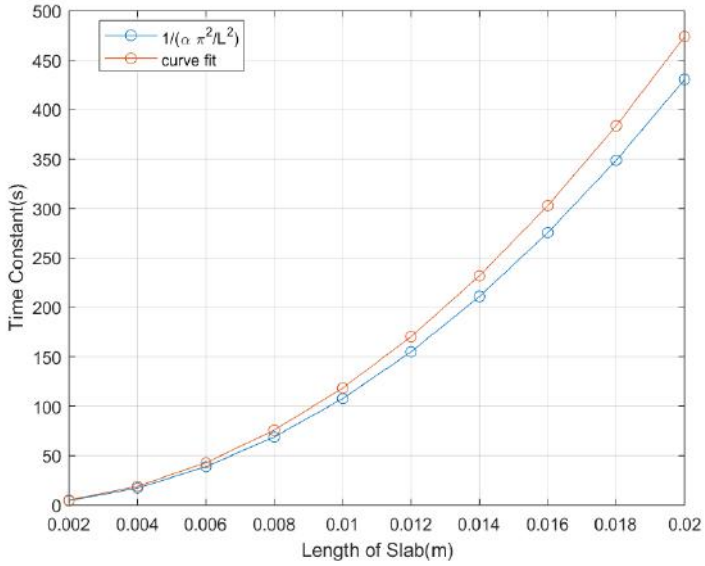

Figure 2.6: Time constant(τ) using the curve fitting(red plot) and term $\frac{L^2}{\alpha\pi^2}$, as function of length of slab

Since the time constant is approximately 550 s for a slab of 20 mm it can be concluded that, if quenching boundary conditions can be applied in real life, it may be hard to build an actuator that is able to have the required bandwidth. So the effect of length of the slab on time constant is further studied and the graph is presented in Figure 2.6. Moreover, Figure 2.6 shows the comparison between the time constants from the curve fitting and the time constants attained from the first term of the series $\frac{\alpha n^2\pi^2}{L^2}\alpha n^2$(where n =1) at different lengths of the slab. The maximum error in graph is 9.2 % at 0.02 m when compared with the time constant attained from curve fitting. For a slab of length 2 mm the time constant is approximately 5.2 s. Moreover, the material properties selected in the simulations is olive oil, selection of materials with better thermal diffusivity can reduce the time constant. However, to apply quenching boundary conditions in practice would require proper and active cooling.

2.3 Sphere

In this section analytical equations representing the heat conduction in a sphere are studied in steady state and transient state. In transient analysis, a similar problem of quenching as was done for a slab is solved along with the problem of a sphere with internal heat generation and convection boundaries. [23] [20, P. 183-250] The sphere with heat generation and convection boundary conditions is expected to closely represent the experimental model.In a 3D sphere The partial differential equation representing the heat conduction of a 3D sphere (in spherical coordinates) is given by [17, P. 76] [20, P. 183]

$$\frac{1}{r^2}\left(\frac{\partial}{\partial r}r^2k\frac{\partial U}{\partial r}\right)+\frac{1}{r^2\sin^2\theta}\frac{\partial}{\partial\phi}\left(\sin\theta k\frac{\partial U}{\partial\phi}\right)+\frac{1}{r^2\sin\theta}\frac{\partial}{\partial\theta}\left(\sin\theta k\frac{\partial U}{\partial\theta}\right)+\dot{e}_{\text{gen}}=\rho c\frac{\partial U}{\partial t} \tag{2.29}$$

where $\dot{e}_{\text{gen}}$ is the heat generated in the body per unit volume (W/m^3), ρ represents the mass density of the sphere, c represents the specific heat, k is the thermal conductivity of the material

of the sphere and α is the thermal diffusivity of the body. U represents the temperature as a function of position and time.

2.3.1 Heat Transfer in a Sphere without heat generation in steady state

We assume a hollow sphere of inner radius r_1 and outer radius r_2. Using the spherical symmetry the problem only depends on r. So, for this 1D problem, assuming steady state analysis, i.e. without heat generation, the spherical heat conduction 2.29 can be written as [22] [17, P. 73].

$$\frac{\partial}{\partial r}\left(r^2 k \frac{\partial U}{\partial r}\right) = 0 \tag{2.30}$$

Considering thermal conductivity k, as constant material property

$$\frac{\partial}{\partial r}\left(r^2 \frac{\partial U}{\partial r}\right) = 0 \tag{2.31}$$

Boundary conditions assumed are

$$U(r_1) = T_1 \tag{2.32}$$
$$U(r_2) = T_2 \tag{2.33}$$

where T_1 and T_2 are the temperatures at boundary r_1 and r_2, respectively.
Integrating the equation (2.30) once results in

$$r^2 k \frac{\partial U}{\partial r} = C_1 \tag{2.34}$$

Integrating the above equation again results in

$$U(r) = -\frac{C_1}{r} + C_2 \tag{2.35}$$

The substitution of the boundary conditions in Equation 2.35 gives

$$U(r_1) = T_1 \rightarrow -\frac{C_1}{r_1} + C_2 = T_1 \tag{2.36}$$
$$U(r_2) = T_2 \rightarrow -\frac{C_1}{r_2} + C_2 = T_2 \tag{2.37}$$

Solving the above equations for C_1 and C_2

$$\begin{aligned} C_1 &= -\frac{r_1 r_2}{r_2 - r_1}(T_1 - T_2) \\ C_2 &= \frac{r_2 T_2 - r_1 T_1}{r_2 - r_1} \end{aligned} \tag{2.38}$$

The temperature as function of the radial position in the sphere is given by

$$U(r) = \frac{r_1 r_2}{r(r_2 - r_1)}(T_1 - T_2) + \frac{r_2 T_2 - r_1 T_1}{r_2 - r_1} \tag{2.39}$$

The heat flux is given by [26, P. 7] [17, P. 18]

$$\dot{Q}'' = -k\frac{\mathrm{d}U}{\mathrm{d}r} = k\frac{r_1 r_2}{r^2[r_2 - r_1]}[T_1 - T_2] \tag{2.40}$$

The heat loss, representative of the total heat conduction through the body surface is (heat rate)

$$\dot{Q}_{\text{loss}} = -kA\frac{dU}{dr} \tag{2.41}$$

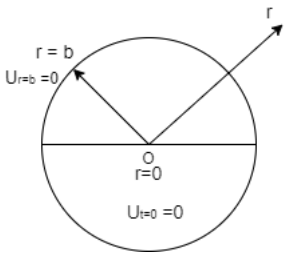

Figure 2.7: Sphere With Imposed Boundary Conditions

After substitution of the area of a sphere and equation 2.38, this becomes

$$\dot{Q}_{\text{loss}} = -k(4\pi r^2)\frac{C_1}{r^2} \tag{2.42}$$

After cancelling r this becomes:

$$\dot{Q}_{\text{loss}} = -4\pi k C_1 \tag{2.43}$$

And after again replacing C_1 from equation 2.38 this becomes:

$$\dot{Q}_{\text{loss}} = 4\pi k r_1 r_2 \frac{T_1 - T_2}{r_2 - r_1} \tag{2.44}$$

2.3.2 Steady state heat conduction in a sphere with internal heat generation

In case of a spherical body transient state analysis, the above equation 2.29 can be simplified to

$$\frac{1}{r^2}\left(\frac{\partial}{\partial r} r^2 \cdot k\frac{\partial U}{\partial r}\right) + \dot{e}_{\text{gen}} = \rho c \frac{\partial U}{\partial t} \tag{2.45}$$

Consider a steady state condition with heat generation, then the temperature is constant with respect to time [22]

$$\frac{1}{r^2}\left(\frac{\partial}{\partial r} r^2 \cdot k\frac{\partial U}{\partial r}\right) + \dot{e}_{\text{gen}} = 0 \tag{2.46}$$

The solution for the differential equation (2.46) is given by [27]

$$U = -\frac{\dot{e}_{\text{gen}} r^2}{6k} + \frac{A}{r} + B \tag{2.47}$$

2.3.3 Sphere Transient Analysis

As done with slab, a quenching problem of a sphere of radius b, shown in Fig2.7, is considered during the transient analysis.
The equation governing the heat flow in a 1D sphere of radius b is given by [23]

$$\frac{1}{r^2}\left(\frac{\partial}{\partial r} r^2 \frac{\partial U}{\partial r}\right) = \frac{1}{\alpha}\frac{\partial U}{\partial t} \tag{2.48}$$

The boundary conditions and initial condition for this situation are

$$\begin{aligned} &U(b,t) = 0 \\ &\left.\frac{\partial U}{\partial r}\right|_{r=b} = 0 \ \ \forall \ \ t > 0 \\ &U(r,0) = f(r) \end{aligned} \tag{2.49}$$

When using separation of variables

$$U(r,t) = R(r)T(t) \tag{2.50}$$

By substituting the above equation in 2.48 and rearranging

$$\frac{1}{r^2 R}\frac{\partial}{\partial r}\left(r^2\frac{\partial R}{\partial r}\right) = \frac{1}{\alpha T}\frac{\partial T}{\partial t} \tag{2.51}$$

Then equating both sides of the above equation 2.51 to $-\lambda^2$ gives

$$\frac{\mathrm{d}T}{\mathrm{d}t} + \lambda^2 \alpha T = 0 \tag{2.52}$$

$$\frac{1}{r^2}\frac{\mathrm{d}}{\mathrm{d}r}\left(r^2\frac{\mathrm{d}R}{\mathrm{d}r}\right) + \lambda^2 R = 0 \tag{2.53}$$

Solving both equations 2.52 gives

$$T(t) = ce^{-\alpha\lambda^2 t} \tag{2.54}$$

$$R(r) = A^{|}\frac{\sin(\lambda r)}{r} + B^{|}\frac{\cos(\lambda r)}{r} \tag{2.55}$$

where $A^{|}$ and $B^{|}$ are constants. Since $B^{|}$ has to be 0 to satisfy $U = 0$ at $r = 0$. Then the boundary condition at $r = b$ (see equation 2.49) yields the following eigenvalues

$$\lambda_n = \frac{n\pi}{b} \tag{2.56}$$

After substitution in equation 2.55, this gives

$$R_n(r) = \frac{A_n^{|}}{r}\sin\left(\frac{n\pi r}{b}\right) \qquad \text{for n=1,2,3...} \tag{2.57}$$

Substitution of 2.54 and 2.57 in 2.50 gives

$$U(r,t) = \sum_{n=1}^{\infty} R_n(r)T(t) \tag{2.58}$$

Which after substitution of the equation 2.52 and 2.57 becomes

$$U(r,t) = \sum_{n=1}^{\infty}\frac{A_n}{r}\sin(\lambda_n r)e^{-\alpha\lambda_n^2 t} \tag{2.59}$$

Where $A_n = A_n^{|}c$ with n=1,2,3.. A_n can be determined from initial conditions

$$U(r,0) = f(r) = \sum_{n=1}^{\infty}\frac{A_n}{r}\sin(\lambda_n r) \tag{2.60}$$

The equation 2.60 is similar to the Fourier series with Fourier's coefficients

$$A_n = \frac{2}{b}\int_0^b f(r^{|})\sin\left(\lambda_n r^{|}\right)r^{|}dr^{|} \tag{2.61}$$

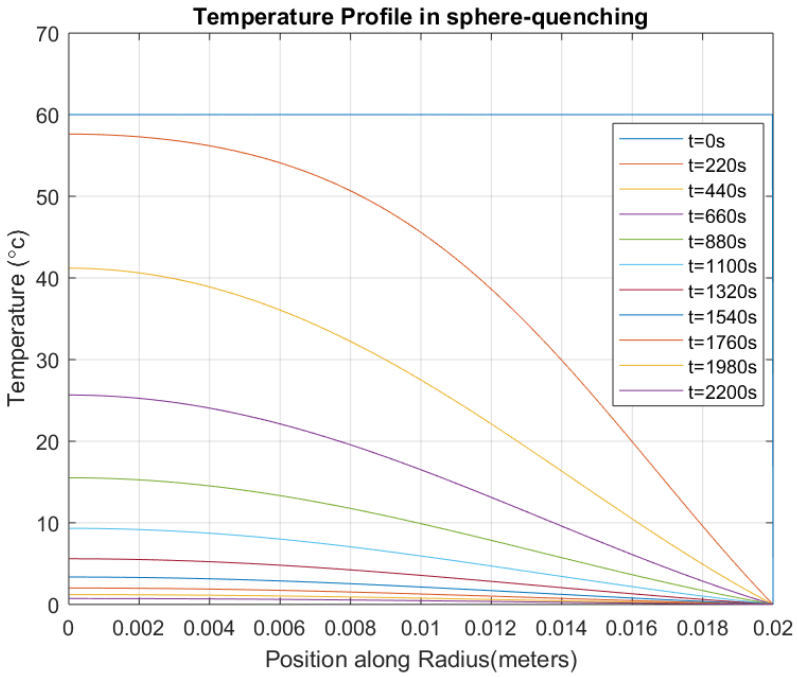

Figure 2.8: MATLAB simulation of transient analysis quenching of sphere, for n =1000

Parameters/Settings	**MATLAB**	**COMSOL**
Radius r in (m)	0.02	0.02
Initial temperature with in Sphere	60 °C	333.15 K
Set temperature at boundaries	0 °C	273.15 K
Thermal Conductivity $\mathrm{W\,m^{-1}\,K^{-1}}$	0.17	0.17
Density $\mathrm{kg\,m^{-3}}$	917	917
Heat capacity in $\mathrm{J\,kg^{-1}\,K^{-1}}$	1970	1970
Thermal diffusivity α ($\mathrm{m^2\,s^{-1}}$)	9.4105×10^{-8}	9.4105×10^{-8}
Simulation end time (s)	2200	2200
n terms	1000	1000

Table 2.3: Sphere with Imposed boundary settings on MATLAB and COMSOL

Matlab results

MATLAB simulation is performed for the sphere with imposed boundary conditions, as is done for slabs, using solutions derived from analytical analysis. Firstly, A_n is calculated using equation (2.61) based on the assumed physical parameters of the sphere and then the final solution is implemented using equation (2.59). The used parameters, resembling the values of olive oil, are shown in table 2.3.
The graph 2.8 represents the temperature profile in a sphere for the imposed boundary problem represented by equation (2.59). The temperature profile along the radius is plotted for every 220 s. In the case of quenching, using the Equation 2.60 the temperature reaches a near 0 °C but not 0 °C. Therefore, the time constant for the system is determined. From graph 2.8, it apparent that the time required for a sphere of radius 0.02 m at 60 °C to reach 22 °C is approximately 700 s. To get a good estimate on the time constant curve fitting is performed the temperature vs time plot obtained when considering the centre of the sphere, this is shown in Figure 2.10.

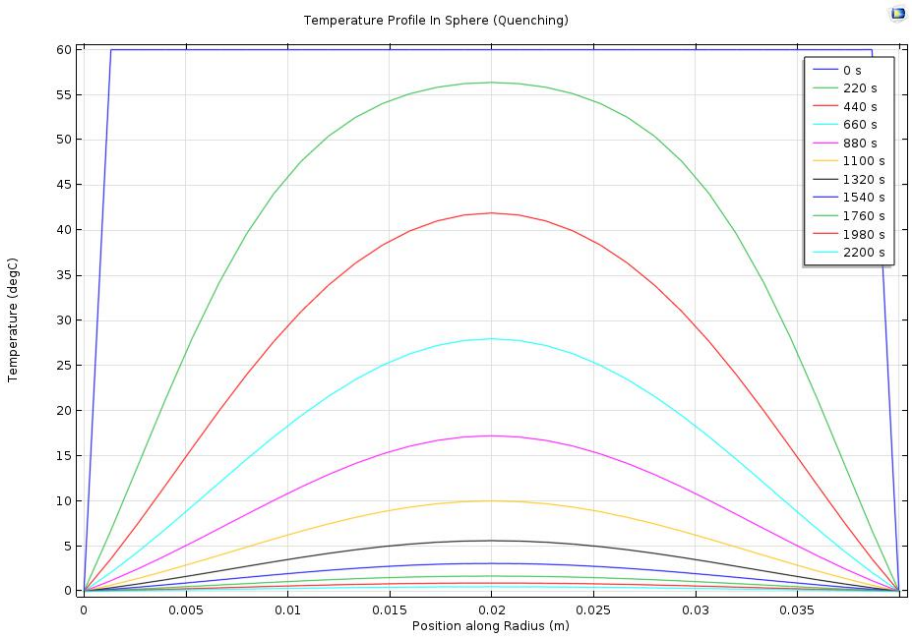

Figure 2.9: COMSOL simulation of transient analysis quenching of sphere.

COMSOL Heat Flow Simulation

The same physical parameters that are used in the MATLAB simulation are used to build the model in COMSOL using the module for heat transfer in solids. The results are obtained through a time-dependent study, analysed for a time period of 2200 s. The graphs are plotted for every 220 s to observe the heat flow at different times as shown in graph 2.9. Furthermore, the temperature profile of the entire volume of sphere at initial condition t =0 s and at t_{end} =2200 s can be clearly observed in 2.11 and 2.12 respectively. The time constant of the model studied is 679.6 s, shown in Figure 2.10.

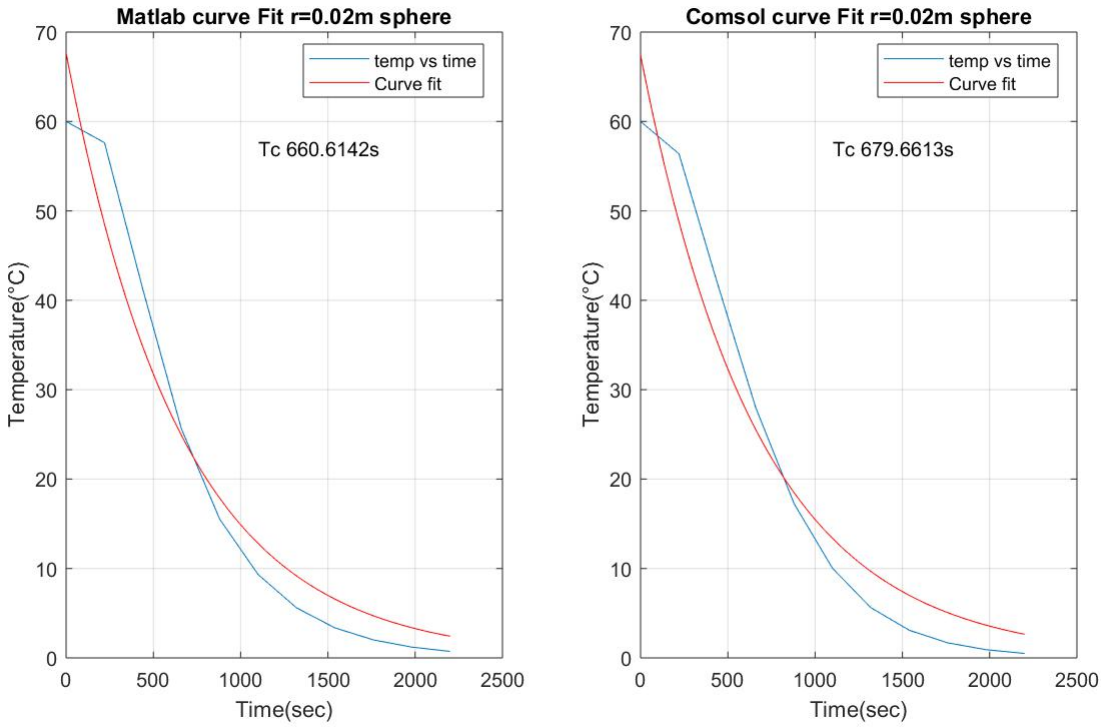

Figure 2.10: Time constant (τ) when temperature plots(blue) at the centre of the sphere in transient quenching situation is curve fitted(red), MATLAB (left side) and COMSOL (right side). Same time points are taken for curve fitting as shown in Figure 2.8 and Figure 2.9

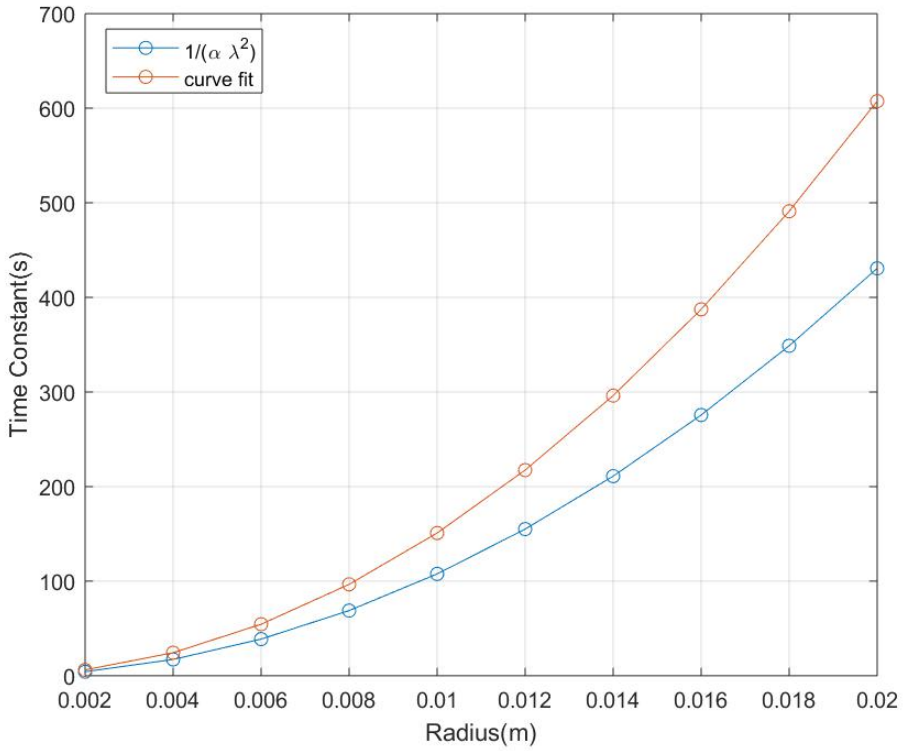

Figure 2.13: MATLAB, time constant obtained from curve fit (red plot) and $\frac{1}{\alpha\lambda^2}$ (blue plot) with change in radius of sphere for transient quenching situation.

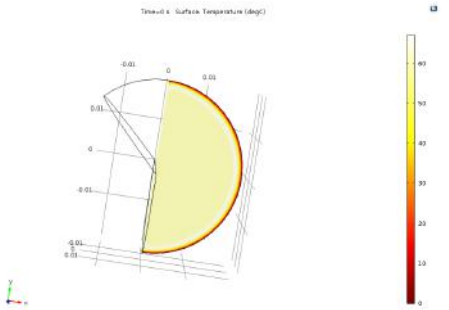

Figure 2.11: COMSOL Temperature profile of Sphere Quenching at t=0 s

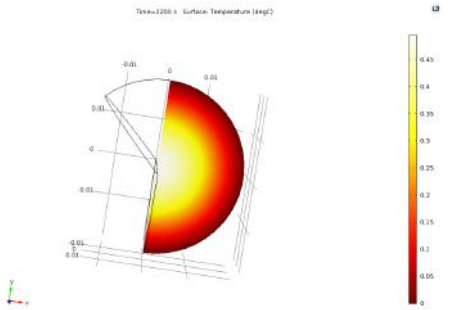

Figure 2.12: COMSOL Temperature profile of Sphere Quenching at t=2200 s

Conclusion

The analytical equations and corresponding MATLAB simulations and the COMSOL model simulations shown in figures 2.8 and 2.9 respectively, show a similar trend in temperature change with position and time. Even though there is a small error of 2.7 % in time constant, since both models show very similar behaviour, it is concluded that they are consistent.

Since the time constant is approximately 660 s it can be concluded that, even if quenching boundary conditions of the sphere can be applied in real life, it would not be feasible to build an actuator that is able to have the required bandwidth without use of any additional cooling. Therefore, it would be interesting to study the effect of radius on the time constant. In Figure 2.13 the time constant with change in radius of a sphere is shown when two different methods to determine time constants are used, namely using curve fitting and other using an approximation $\frac{1}{\alpha\lambda^2}$. These plots show that with lower radius a better cooling time constant can be achieved. The maximum error in the graph 2.13 at 0.02 m (approximately at 29 %) can be due to the significant decrease in the λ_n value with increase in radius which makes the λ value change significantly for values of $n > 1$.

2.3.4 Transient analysis of sphere with internal heat generation

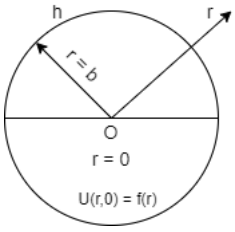

Figure 2.14: Transient case of sphere with internal heat generation, indicating the initial condition.

A solid sphere of radius 'b' and initial temperature $f(r)$ is considered as shown in figure 2.14. For $t > 0$, there is heat convection at boundary $r = b$ with a convection coefficient of h. The heat generation is considered as uniform heat generation in the sphere. From equation 2.29, the 1D governing equation in r for the particular condition can be written as [20, P. 203]

$$\frac{1}{r^2}\left(\frac{\partial}{\partial r}r^2 k\frac{\partial U}{\partial r}\right) + \dot{e}_{\text{gen}} = \rho c\frac{\partial U}{\partial t} \tag{2.62}$$

Where,

- r represents the position along radius of sphere.

- U represents the temperature as a function of position and time $U(r,t)$.
- k is thermal conductivity
- $\dot{e}_{\text{gen}}$ (represented later by g_o) uniform heat generation in the sphere per unit volume.(in $\mathrm{W m^{-3}}$)
- ρ mass density of the sphere
- c is the Specific heat capacity of material of the sphere
- t is time.

The above equation 2.62 can be written as

$$\frac{\partial^2 U}{\partial r^2} + \frac{2}{r}\frac{\partial U}{\partial r} + \frac{g_{\text{o}}}{k} = \frac{1}{\alpha}\frac{\partial U}{\partial t} \tag{2.63}$$

where α is the thermal diffusivity, given by $\alpha = \frac{k}{\rho c}$ and $\dot{e}_{\text{gen}} = g_{\text{o}}$.
Boundary conditions considered in this derivation are as follows:

$$U(r \to 0) \implies \text{finite} \quad \text{and} \quad -k\frac{\partial U}{\partial r}\bigg|_{r=\text{b}} = hU(b,t) \tag{2.64}$$

The initial condition that is used is:

$$U(r,0) = f(r) \tag{2.65}$$

To effectively solve the partial differential equation in spherical coordinates the transformation $T(r,t) = rU(r,t)$ is introduced. This reduces the equation (2.63) into a similar Cartesian heat equation which can be solved. [20, p. 194]
Because of the introduced transformation the partial differential equation (2.63), boundary conditions (2.64) and the initial condition change accordingly. [20, P. 196,204]

$$\frac{\partial^2 T}{\partial r^2} + \frac{g_{\text{o}} r}{k} = \frac{1}{\alpha}\frac{\partial T}{\partial t} \tag{2.66}$$

Boundary conditions are transformed to,

$$T(0,t) = 0 \quad \text{and} \quad \frac{\partial T}{\partial r} + \left(\frac{h}{k} - \frac{1}{b}\right) T = 0 \quad \text{at} \quad r = b \tag{2.67}$$

The initial condition is transformed to

$$T(r,0) = r f(r) \tag{2.68}$$

Equation (2.66) is non-homogeneous and therefore can be solved by using superposition transformation $T(r,t) = \Psi(r,t) + \Phi(r)$.
Where $\Phi(r)$ is a non-homogeneous Ordinary differential equation and $\Psi(r,t)$ is a homogeneous partial differential equation and boundary conditions are transformed.
Solving $\Phi(r)$ which is a 1D problem:

$$\frac{\partial^2 \Phi}{\partial r^2} + \frac{g_{\text{o}} r}{k} = 0 \quad \text{in} \quad 0 \le r < b \tag{2.69}$$

Using boundary condition from equation 2.67, they transform to,

$$\Phi(r=0) = 0 \quad \text{and} \quad \frac{\mathrm{d}\Phi}{\mathrm{d}r} + K\Phi = 0 \quad \text{at} \quad r = b \tag{2.70}$$

Where

$$K = \frac{h}{k} - \frac{1}{b} \tag{2.71}$$

Integrating equation (2.69) twice, to form a particular solution

$$\Phi(r) = C_1 + C_2 r - \frac{g_o}{6k} r^3 \tag{2.72}$$

By substituting boundary conditions from (2.70),

$$C_1 = 0 \qquad \text{and} \qquad C_2 = \left(\frac{b g_o}{6h}\right)\left(2 + \frac{hb}{k}\right) \tag{2.73}$$

Therefore the particular solution for $\Phi(r)$

$$\Phi(r) = r\left(C_2 - \frac{g_o}{6k} r^2\right) \tag{2.74}$$

Now the homogeneous PDE $\Psi(r,t)$ needs to be solved to find the total solution. The equation (2.66) transforms as

$$\frac{\partial^2 \Psi}{\partial r^2} = \frac{1}{\alpha}\frac{\partial \Psi}{\partial t} \qquad \text{in} \qquad 0 \le r < b \quad t > 0 \tag{2.75}$$

Using boundary condition and initial condition from equation 2.67, they transform to,

$$\begin{aligned} \text{Boundary conditions: } \Psi(0,t) = 0 \quad \text{and} \quad \frac{\mathrm{d}\Psi}{\mathrm{d}r} + K\Psi = 0 \quad \text{at} \quad r = b \\ \text{Initial condition: } \Psi(r,0) = r f(r) - \Phi(r) \end{aligned} \tag{2.76}$$

Using the separation of variables,

$$\Psi(r,t) = R(r)\Gamma(t) \tag{2.77}$$

Substituting the above equation in (2.75) and separating the equation in terms of R and Γ.

$$\begin{aligned} \frac{1}{R}\frac{\mathrm{d}^2 R}{\mathrm{d}r^2} &= \frac{1}{\alpha\Gamma}\frac{\mathrm{d}\Gamma}{\mathrm{d}t} \\ \frac{1}{R}\frac{\mathrm{d}^2 R}{\mathrm{d}r^2} &= -\lambda^2 \\ \frac{1}{\alpha\Gamma}\frac{\mathrm{d}\Gamma}{\mathrm{d}t} &= -\lambda^2 \end{aligned} \tag{2.78}$$

Solution of the differential equation in t gives:

$$\Gamma(t) = C_1 e^{-\alpha\lambda^2 t} \tag{2.79}$$

Solution of the differential equation in r gives:

$$R(r) = C_2 \cos(\lambda r) + C_3 \sin(\lambda r) \tag{2.80}$$

Using the boundary conditions from (2.76), $C_2 = 0$, therefore,

$$R(r) = C_3 \sin(\lambda r) \tag{2.81}$$

The following transcendental equation is obtained from the second boundary condition:

$$\lambda_n \cot \lambda_n b = -K \quad \rightarrow \quad \lambda_n \quad \text{for} \quad n = 1,2,3,... \tag{2.82}$$

The solution of ODE (2.76) is,

$$\Psi(r,t) = \sum_{n=1}^{\infty} C_n \sin(\lambda_n r) e^{-\alpha {\lambda_n}^2 t} \qquad \text{where} \quad C_n = C_1 C_3 \tag{2.83}$$

Parameters/Settings	**MATLAB**	**COMSOL**
Radius b (m)	0.02	0.02
Initial temperature with in the sphere	0 °C	273.15 K
Convection coefficient h (W/m^{2}K)	10	10
Uniform heat generation g_o (Wm^{-3})	2.6857×10^4	2.6857×10^4
Thermal Conductivity k (Wm^{-1}K^{-1})	0.17	0.17
Density ρ (kgm^{-3})	917	917
Heat capacity c (Jkg^{-1}K^{-1})	1970	1970
Thermal diffusivity α (m^{2}s^{-1})	9.4105×10^{-8}	9.4105×10^{-8}
Simulation end time t_{end}	5000 s	5000 s
n terms	2001	2001

Table 2.4: Sphere with Internal Heat Generation settings on MATLAB and COMSOL

Using the initial condition

$$\Psi(r,0) = rf(r) - \Phi(r) = \sum_{n=1}^{\infty} C_n \sin(\lambda_n r) \tag{2.84}$$

By using the operator below, the Fourier coefficient C_n is solved

$$* \int_{r=0}^{b} \sin(\lambda_q r) dr \tag{2.85}$$

The value of C_n is

$$C_n = \frac{\int_{r=0}^{b} [rf(r) - \Phi(r)] \sin(\lambda_n r) dr}{\int_{r=0}^{b} \sin(\lambda_n r) dr} \tag{2.86}$$

The final solution $U(r,t)$ is obtained by

$$U(r,t) = \frac{T(r,t)}{r} \quad \text{and} \quad T(r,t) = \Psi(r,t) + \Phi(r) \tag{2.87}$$

This gives

$$U(r,t) = \sum_{n=1}^{\infty} C_n \frac{\sin(\lambda_n r)}{r} e^{-\alpha \lambda_n^2 t} + \left(C_2 - \frac{g_o}{6k} r^2\right) \tag{2.88}$$

Matlab Results

MATLAB simulations are done for the sphere with convective boundary and uniform internal heat generation condition, by using the solutions from the obtained analytical solutions. Firstly, the C_n values are calculated using equation (2.86) based on the assumed physical parameters of the sphere, and then the final solution is implemented using the equation (2.88). The parameters used in calculations are shown in table 2.4.
The graph 2.15 represents the temperature profile in a sphere with the convective boundary with internal heat generation problem represented by equation 2.88. The temperature profile of a sphere of radius of 0.02 m when heated for 5000 s is simulated. At this time it can be stated that, an approximate equilibrium is obtained between heat loss due to convection and heat generation, though there will be very small changes in temperature. Once the equilibrium is attained the body remains at that temperature until there is external physical interference's or change in heat generation output. From the graph 2.15, its apparent that time required for a sphere of radius 0.02 m at 0 °C to reach a maximum temperature is approximately 5000 s. When a temperature vs time graph is plotted for the position, centre of the sphere, the time constant attained from the the curve fitting is approximately 1600 s.

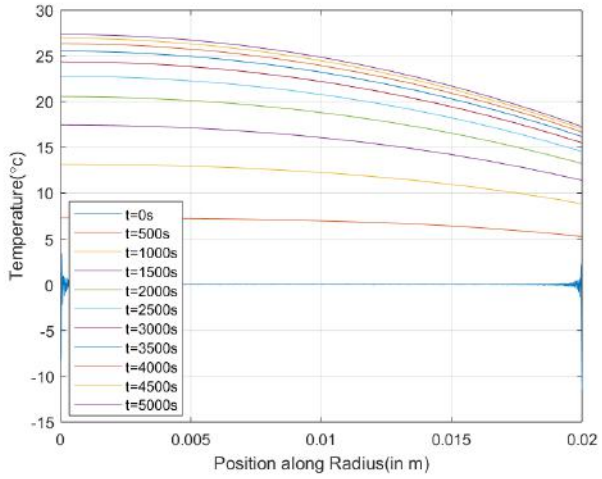

Figure 2.15: MATLAB simulation of sphere with internal heat generation and convective boundaries, plotted in time intervals of 500 s for t=5000 s (for n =2001)

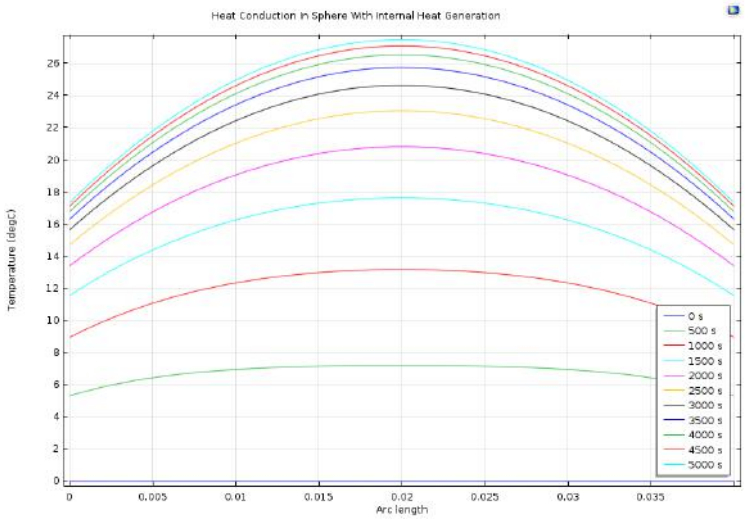

Figure 2.16: COMSOL simulation of sphere with internal heat generation and convective boundary, plotted in time intervals of 500 s for t=5000 s

COMSOL heat flow simulation

The physical parameters that are used in the MATLAB simulation are used as well to build the model in COMSOL using heat transfer in Solids module. The results are obtained through time-dependent study analysed for a time period of 5000 s and graphs are plotted for every 500 s to observe the heat flow at different times as shown in graph 2.16. The temperature profile of the entire volume of the sphere at the initial condition t =0 s and after almost reaching the maximum temperature at t_{end} =5000 s can be clearly observed in 2.17 and 2.18 respectively. The time constant that is attained from the graph is, 1585.72 s shown in Figure 2.19.

Conclusion

The analytical model as used in the MATLAB simulations and the COMSOL model simulations shown in figures 2.15 and 2.16 respectively show a similar trend in temperature change with position and time. The maximums from both graphs are approximately identical. This helps in cross verification of the analytical equation with the COMSOL model. Moreover, the time vs temperature at the centre of the sphere is plotted from both the MATLAB and COMSOL simula-

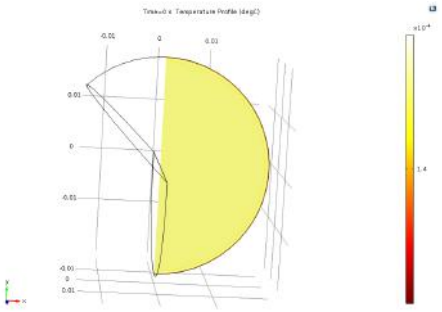

Figure 2.17: COMSOL Temperature profile of Sphere with internal heat generation at t=0s.

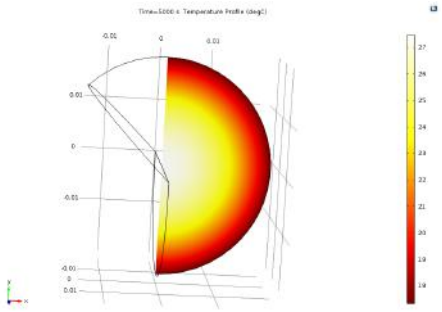

Figure 2.18: COMSOL Temperature profile of Sphere with internal heat generation at t=5000 s

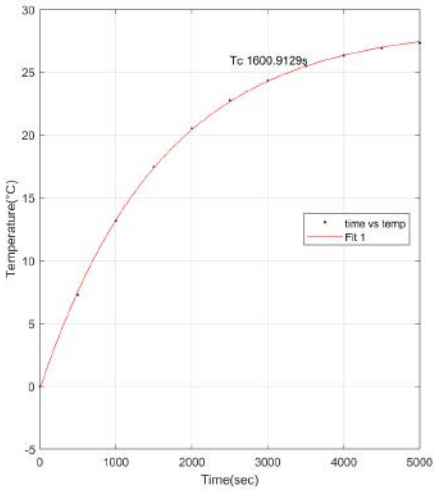

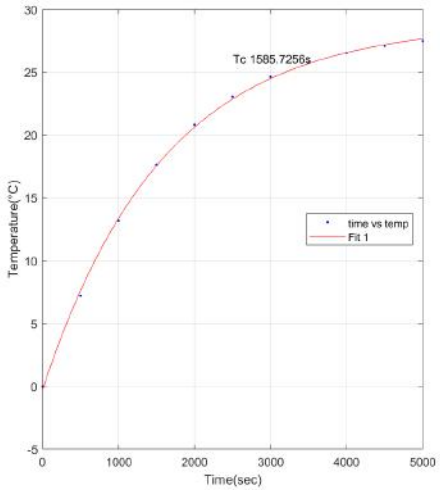

Figure 2.19: Time constant (τ) when temperature plots(blue) at the centre of the sphere in transient heating situation is curve fitted(red), MATLAB (left side) and COMSOL (right side). Same time points are taken for curve fitting as shown in Figure 2.15 and Figure 2.16

tions and time constants are determined using curve fitting for better approximation, these are presented in Figure 2.19. The error in time constant is 0.94 % when compared to the MATLAB simulation. Since both models show similar behaviour in time and space, it is deduced that they are consistent.

Since the time constant is approximately 1600 s shown in Figure 2.19, it can be concluded that convective boundary conditions with heat generation can be applied in real life, it would be feasible to build an actuator but it would be hard to acquire the required bandwidth with the given radius and thermal diffusivity of the material. Moreover, to apply these boundary conditions in practice would require proper uniform heating and cooling (uniform external temperature). Therefore, to further study the relation between the radius and time constant a graph is plotted as shown the time constant attained with curve fitting Figure 2.19. This graph can help in determining the radius for the required time constant.

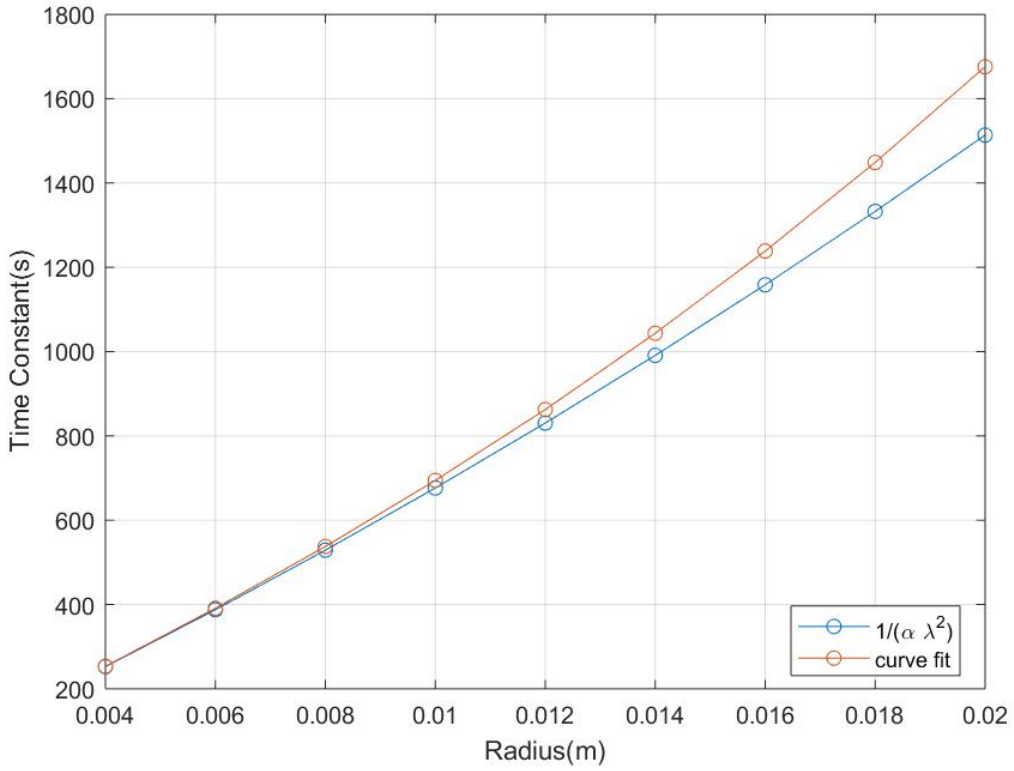

Figure 2.20: MATLAB, time constant obtained from curve fit (red plot) and $\frac{1}{\alpha\lambda^2}$ (blue plot) with change in radius of sphere for transient internal heating with convective boundaries situation.

2.4 Discussion

In the method of one term approximation in [17], only the first term of the infinite series i.e., the first definite value of λ is used in transient analysis to get the temperature in a body with respect to position and time. Using this approximation, the time constants from the curve fitting simulations are compared to the first term of $\frac{1}{\alpha\lambda^2}$ using only the first definite value of λ as shown in Equation 2.88 and a graph is plotted as shown in Figure 2.20. The Figure 2.20 shows that at a radius of 0.02 m the maximum error in time constant from first term approximation is 9.6 % when compared to time constant from curve fitting, and this error decreases with decrease in radius of the sphere. Therefore, this term can also be used in the (first) estimation of the time constant at lower radii without the use of curve fitting.
When the time constants in Figure 2.10 and Figure 2.19 are compared to the required switching time of 1.5 s (as mentioned in section 1), in case of sphere quenching a sphere of radius 0.002 m have a time constant of 1.55 s as shown in Figure 2.13 i.e., for the actuator of radius 0.002 m requires 1.55 s to reach 36.7 % of the initial maximum temperature. Figure 2.20 shows the tome constant dependency on radius during heating. Based on this it can be seen that there are stringent requirements on the radius of the actuator to attain the required switching time during heating or cooling. As for the heating, the required temperature gradient can be controlled with the maximum temperature reached which is a function of input power, but the power (and the maximum temperature) that is required to attain the set gradient will be higher with increasing time constant. Though these analytical solutions give a good approximation on the actuator design in ideal conditions some of the factors like change in thermal conductivity and density due to change in temperature are not included.

2.5 Conclusion

In this chapter analytical analyses were done in 1D steady state and 1D transient situations in both slab and sphere geometries. The analytical solutions from the study are implemented using MATLAB and the simulations are furthermore compared with FEM (COMSOL) simulations. From these simulations the time constants are determined which are representative of the response time of a potential actuator of approximately same size. Furthermore, the time constants obtained from MATLAB and COMSOL model simulations are approximately equal as shown in Figure 2.10 and Figure 2.19. In both cases there is a percentage error of less than 3 % in the time constant from MATLAB when compared to COMSOL. Which allows the conclusion that the analytical model and FEM model are consistent.
It is speculated that to built the actuator the radius of the actuator needs to be as small as possible and suitable materials are required in the process to design a reliable actuator for the determined application. To study the functioning of the actuator in real time a physical model needs to be designed and fabricated and experiments need to be conducted.

3 Design

This chapter focuses on the various design decisions made regarding the model and material selection for 3D printing of these designed models. Different ideas for the design of the actuator along with the motivation for the test design are discussed in this section.

3.1 Concepts

3.1.1 Solid Block Heating

Figure 3.1: Design Sketch for solid block heating with; solid block(in red color), flexible membrane (in blue color) and casing(in black color)

In this concept, the idea is to use a solid block that expands(or contracts) on heating(or cooling). The linear expansion of the solid block due to heating will expand the membrane and contracts when the solid cools down again. Since the temperatures from the heater might be higher than the normal human body temperature, it is important to avoid any direct contact between the heater and the human body. For this model to work, there are important requirements on materials for 3D printing.

- The material should have a higher linear expansion coefficient at low temperature changes to meet the actuator requirements.
- A Flexible and non-porous material is required as a membrane.
- The solid block material ideally should also be conductive, so that the material can act as heater itself. If not, an external heater is required.
- The material should be 3D printable.

The advantage of this model is that, since all the parts are solid, it is easy to 3D print provided appropriate materials with the required properties are available. It is easy to handle(or use) since there are no parts that need critical handling. The commonly used 3D printed materials and their properties can be seen in [1]. Some of the 3D print materials with their thermal expansion coefficient and specific heat capacity are presented in Table 3.1. From this table, the highest thermal expansion coefficient is of Thermoplastic Polyurethane (TPU) with $157\,\mu m\,m^{-1}\,^{\circ}C^{-1}$. The heat deflection temperature is low but for the application as an actuator it is reasonable to keep the temperature within these limits. However, when the a TPU block of length 100 mm is heated from 20 °C to 60 °C (ΔT =40 °C) a change in length due to thermal expansion is 0.6 mm, refer to Equation A.1 [28].

From this simple calculation, it is apparent that using the materials in the Table 3.1, it is hard to realise an actuator with the prescribed requirements even after neglecting the linear expansion of casing material due to heating. Therefore, this particular design concept cannot be implemented so a different design concept is required.

S.no	Material	Coefficient of Expansion $\mu m\, m^{-1}\, °C^{-1}$	Heat deflection temperature °C	Specific Heat $J g^{-1}\, °C^{-1}$
1	PLA [29]	68	52	1.8
2	ABS [30]	90	98	1.6 - 2.1
3	Nylon [31]	95	80-95	1.8
4	Polypropylene [32]	150	121	1.92
5	TPU	157	60-74	1.7-1.9

Table 3.1: Thermal properties of commonly used 3D print materials [1]

3.1.2 Block in the centre design

In this concept, a porous solid block is placed in the actuator which can expand when heated and contract when cooled, by the use of a fluid, as shown in Figure 3.2. The fluid is heated through a heater, which heats the solid block via convection and conduction. The solid block can be any 3D printable material that has a high thermal expansion coefficient and the solid block being porous increases the surface area for heat transfer. Due to the heating of fluid and solid, there will be a thermal expansion of both materials therewith causing the expansion of the membrane. However, this design has the same drawbacks as the previous design, such as the minimal thermal expansion of solid 3D printable materials available and the need for an external heater in addition to the block.
Though the motivation for the usage of solid material in actuation is due to the ease of 3D printing and handling with solid materials, there is an increase in the number of parts due to inclusion of the additional heater. To avoid the use of the additional heater the porous block may be used as heater, however, support structures are required to 3D print the porous block as shown in Figure 3.2. Moreover, since fluids (for example refer Table 3.2) have a higher thermal expansion than solids (refer Table 3.1), the actuation due to volume expansion of solid block is lower than that of fluid, it is preferable to remove the porous block and substitute it with fluid to improve the design's performance. Therefore, a different and standard design is considered.

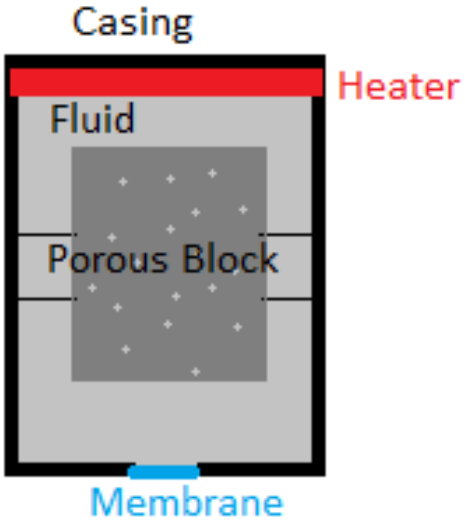

Figure 3.2: Design Concept of block in centre design; heater (in red color), flexible membrane (in blue color), casing (black color), porous block (in dark grey color with white dots) and fluid (in grey color)

3.1.3 Directly heating a Fluid

In this concept, there will be no solid block as shown in Figure 3.3 but a heater is placed just for the purpose of heating the fluid in the actuator. When the fluid is heated, the volumetric expansion of the fluid induces a pressure that causes hydraulic deformation of the membrane. This design is simple compared to the design in Figure 3.2 therefore it should be easily 3D printable.
In this design, the important factors are the heater, membrane and fluid used. The heater used in this model should be 3D printable and can generate the required heating conditions. The fluid in this model may be either a gas or a liquid, but liquids are preferable because they are easier to handle than gases, and gas design are more challenging than liquid design designs. Therefore, further investigation is required to select the materials that are best suitable for the optimum working of the actuator.

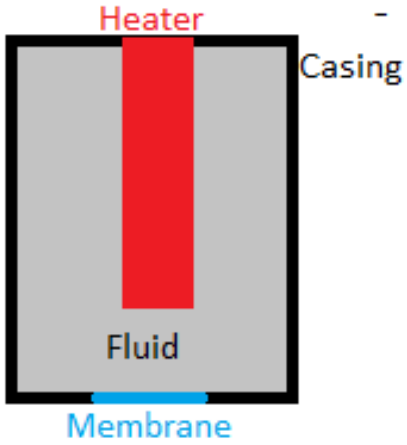

Figure 3.3: Design Concept of directly heating a fluid; heater (in red color), casing in (black color) and flexible membrane (in blue color)

3.1.4 Conclusion

The design concept of directly heating the fluid is chosen as a feasible concept because of the simplicity of the design and the feasibility of 3D printing. Since these choices are mainly motivated by the properties of common materials available for 3D printing; if any other materials that provide better properties in terms of thermal expansion coefficient become available, more appropriate design considerations can be made. In this design it is important to make sure the volumetric expansion of fluid due to change in temperature is high enough to actuate the membrane to block the pneumatic tube of radius 2 mm. It is important that the thermal expansion of the fluid should be higher than the casing(container) and the effective volume change is required for the actuation of the membrane.

3.2 Fluid

While selecting the fluid, the important properties are a high coefficient of thermal expansion, high thermal conductivity and low specific heat. When compared to gases a liquid is chosen as a better option in the design due to its ease of handling, particularly during the design testing process. The force exerted due to the expansion of the liquid with change in temperature allows the membrane to expand. As liquids can be considered incompressible at normal pressures, the volume change inside the actuator due to the expansion of the liquid is directly proportional to the change in volume underneath the membrane. Furthermore, the fluid used should be environmentally friendly and not have any adverse effects on the human body.
When the force required for the deformation of the membrane is higher than the force due to

the expansion of liquid then the pressure within the actuator increases. Moreover, the liquid selected should be filled in without any air gaps in a closed model so to ensure the efficiency of the model.
Some of the approximate liquid properties are mentioned in Table 3.2 [33] [34] [35] . Though Novec7000 has good properties the boiling point is at 34 °C at 1 atm pressure, which can be a good choice in case of phase-change actuators [36].

S.no	Fluid	Thermal Expansion Coeff (at 20 °C-25 °C) (in $°C^{-1}$)	Specific Heat (in $J g^{-1} °C^{-1}$)	Boiling point (in °C)
1	Water	2.1×10^{-4}	4.18	100
2	Olive oil [37] [38, 356]	7×10^{-4}	2	180
3	Silicone transformer oil	10.4×10^{-4}	1.51	150 - 400
4	Novec 7000 [36]	21.9×10^{-4}	1.3	34

Table 3.2: Expansion coefficient and Specific heat table

3.3 Casing

The role of the casing is to provide a robust support to the actuator design and to hold the membrane and the heater, with minimum change in size when heated. The shape of the casing design is selected to be a cylinder based on the application, as the actuator is to be placed within the insertion tubes of endoscopy which are already having cylindrical supply lines it would be easy to fit. Furthermore, if a cuboid shape is selected there is the possibility that the sharp corners might damage the insertion tube.

3.3.1 Casing Material(s)

The available 3D printable materials for the casing are PLA, ABS and Nylon. These materials, as commonly used for prototyping, are taken into consideration for the outer casing. Some properties of PLA, ABS and Nylon can be found in Table 3.1.

Nylon:

A test print is made with Nylon (DSM novamid ID 1030). The advantage of nylon is that it is lighter and provides good adhesion with protopasta. But the material is hygroscopic. Due to this Nylon cannot be used in the actuator design.

ABS:

ABS is also another commonly used material for prototyping. ABS is a rigid material and lighter than PLA but requires a high temperature for printing which makes it prone to warping. [39]

PLA:

As a commonly used material for FDM (fused deposit modelling) 3D printing, PLA is easy to 3D print. High-resolution prints can be obtained by using PLA. The advantage of PLA is that it is stiff and strong when compared to ABS [40]. The melting point of PLA is around 150-160 °C with a heat deflection temperature of 55 °C approximately. [1]
PLA is chosen as the material for the casing, mainly because of the relative ease of 3D printing when compared to ABS. Moreover, the thermal expansion coefficient of PLA is lower than that of ABS so there will be a minimum change in volume when there is a change in temperature.

3.4 Heater

The most important part of the actuator is the heater as the actuation itself depends on the thermal properties of the heater used. The most important thermal properties are thermal conductivity, heat capacity and electrical resistance of the material. Furthermore, the heater used should be able to withstand the temperatures the actuator is designed for.

3.4.1 Heater Material

The 3D printable filaments that are available and suitable as a heater are carbon black filled TPU called PI-ETPU and carbon-infused PLA called protopasta.
There is fairly limited data on the thermal properties of these two materials. Therefore, based on the better 3D print quality with the selected casing material. The material for heater is selected.

PI-ETPU

PI-ETPU is electrically conductive TPU(Thermoplastic polyurethane). This filament is TPU infused with carbon black [41]. PI-ETPU is a flexible material when compared to proto-pasta. Based on the experience gained from the 3D printed designs, it was concluded that the adhesion of PI-ETPU with PLA is not reliable.

Proto pasta

The type of Proto-Pasta used is electrically conductive PLA. It is PLA infused with carbon black (around 22 %) which gives electrical conductivity to the material [42]. As this filament mostly contains PLA it has good adhesion properties with PLA which is used as casing material.

Heater shape

The heater is printed using Electrically conductive PLA. When modelling the actuator the important factor is the design of the heater. The heating capacity of the heater depends on the shape and size of the heater. As the size of the actuator is limited the shape used is important and a trade-off between various factors is required. Due to limited time, some simple structures like cylinder and cuboid are assumed for the design of the heater.

3.4.2 Conclusion

Proto-pasta is chosen as the material for the heater, because of the better print quality with PLA due to better layer to layer adhesion when compared to PI-ETPU. Due to the limited knowledge on analytical equations for various structures a cylindrical structure is assumed for the heater. For order of magnitude estimates on time constant a cylinder of limited length can be approximated by a sphere of comparable size, with strongly resembling boundary conditions as presented in equation Equation 2.64. Further study on suitable parameters for the design of the heater is done in section Section 4.2.

3.5 Membrane

Ninjaflex is used as the material for the membrane because of its good adhesion with PLA, which acts as a casing and also holds the membrane. Ninjaflex is a TPU that provides good flexibility and also durability. [43] [44]

3.6 Designs

3.6.1 Actuator

A preliminary design is made to study the design feasibility with the selected materials. The design of the model is shown in Figure 3.4. In this design, PLA is used for the casing, ninjaflex

for the membrane and gasket and protopasta for the heater. The design consists of two parts; one part is formed by the casing with the membrane and the other part consists of a lid to cover the casing and a heater. Two individual parts are designed due to the limitation of the available dual filament 3D printer (Flashforge creator pro). Two 3 mm screw holes are made on the casing ninjaflex layer and top part to screw them together. A ninjaflex layer is printed on top of the casing to provide better grip and to hold the liquid inside. This design is just made to study the design feasibility.

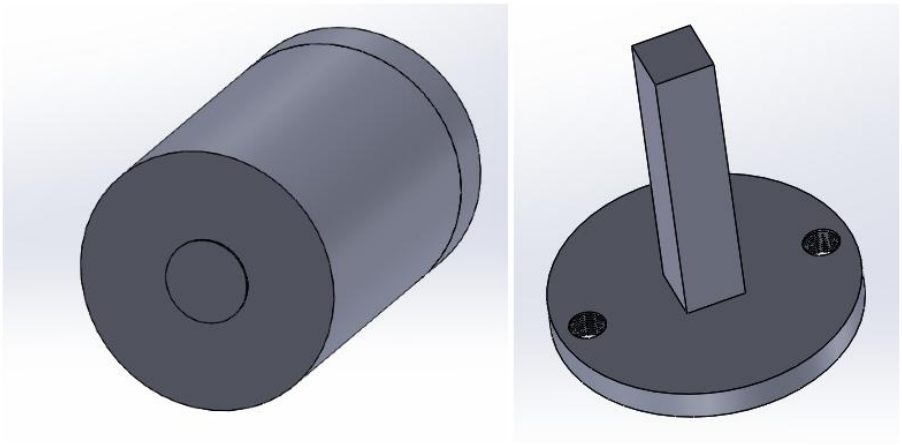

Figure 3.4: Solidworks design; casing with membrane (on left side) and top with heater (on right side)

3.6.2 Open top actuator

The current design is used only to study heat conduction. Since it is hard to study the heat conduction in closed structures an open design is made to be able to study the heat distribution in the actuator. The model design can be seen in Figure 3.5. In this design a cylinder casing with a cylindrical heater at the centre is present. The casing has an external radius of 18 mm, the thickness of 2 mm (also at base) and depth of 10 mm. The heater has a radius of 2 mm and height of 14 mm, furthermore, the bottom of the heater is designed as shown on the right-side of Figure 3.5 to avoid any leaking of liquid. The height of the heater is higher than the casing height so that it can be clamped to provide proper contact with the power supply. This design will be referred to as 'V1' in the rest of the report and the dimensions of the casing and the heater with their total volume is clearly represented in Table 3.4 and Table 3.3.

3.6.3 Enlarged open-top actuator

After the open top actuator shown in Figure 3.5, a second design was made by scaling the effective dimensions of the design shown in Figure 3.5 by a factor of two. The casing has an external radius of 34 mm, thickness of 2 mm (also at base) and depth of 20 mm. The heater has a radius of 4 mm and a height of 26 mm.The motivation to print an open top actuator is to verify the change in time constant as discussed in Section 2.5. This design will be referred to as 'V2' in the rest of the report and the dimensions of the casing and the heater with their total volume is clearly represented in Table 3.4 and Table 3.3.

Design	Outer radius(mm)	Wall thickness (mm)	Casing height (mm)	Volume (mm^3)
V1	18	2	12	≈ 12214
V2	34	2	22	≈ 79897

Table 3.3: Casing parameters of designs V1 and V2

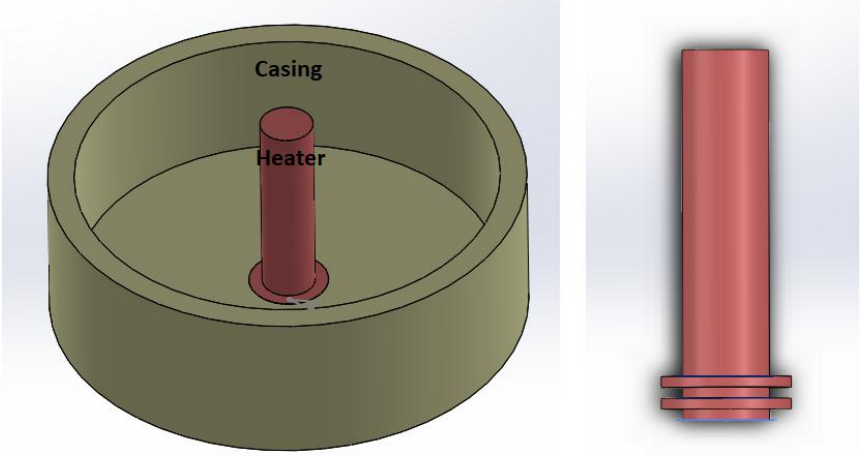

Figure 3.5: Open top actuator with heater design (on the right side)

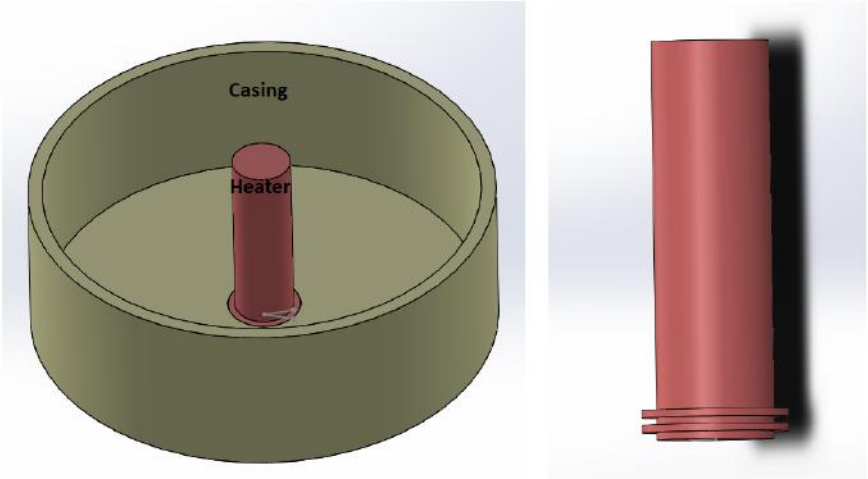

Figure 3.6: Enlarged open top actuator and heater design (on right side)

Design	Heater radius (mm)	Heater height (mm)	Volume (mm^3)
V1	2	14	≈ 176
V2	4	26	≈ 1307

Table 3.4: Heater parameters of designs V1 and V2

3.7 Interfacing

To conduct the required experiment the design is made as an open-top so that the thermal camera can capture the temperature of the olive oil without any obstruction. The heater in the shape of a cylinder is extended through the bottom of the cylinder so that connection can be given at the bottom and the height of the heater is designed to be 2 mm higher than the PLA casing, so that a clamp can hold the ends of the heater and provide the power supply to the heater. The heater ends are coated with conductive silver to reduce the contact resistance between the copper strips and ends of the heater. A test design is placed between the clamps such that the heater top and bottom are connected through copper strips which are soldered

with a wire, as shown in Figure 3.7. These wires are used for connecting to the external power supply.

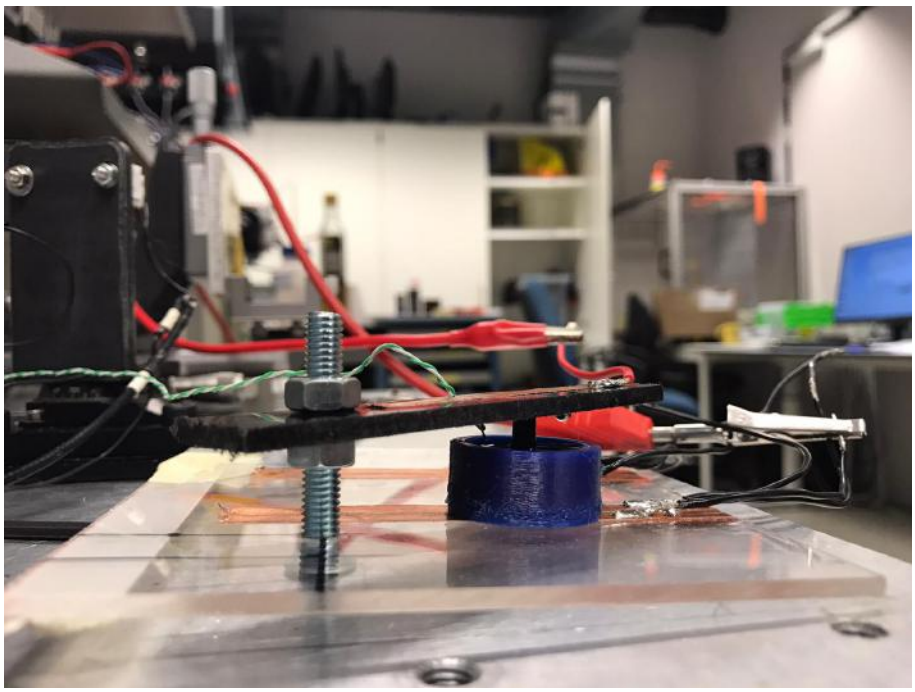

Figure 3.7: Open top actuator measurement setup with connections

3.8 Conclusion

The current design of the actuator consists of a heater that is 3D printed using protopasta, a membrane that is printed by ninjaflex and a casing for the whole actuator that is printed using PLA. Though olive oil is being used for testing, design can also be suitable for a phase change actuator if the fluid like 3M Novec7000 is used and the design is airtight. The actuator is electrically controlled so the power is supplied to the heater by using conductive silver. The fabrication procedure and print settings are discussed in section 4. Even when the design can be printed with the chosen materials, whether or not the actuator functions to match the requirements is an important question. To further explore this , experiments are done to study the heater and heat conduction in the fluid using the heater which is later discussed in section 5. Although membrane properties are important, no further experiments have been done to study the membrane and its properties due to time constraints.

4 Fabrication

This chapter explains the fabrication procedure and settings for various 3D prints used through the experiment.

4.1 Test Design Prints

The designs are 3D printed using the Flashforge creator pro 3D-printer which can print up to 2 different filaments. [45] As the actuator cannot be printed in one (as a single print) because of limitations of the 3D printer, two parts are printed which contribute to the final design. To inspect the 3D printing properties like adhesion between different materials and various print settings, some test designs are 3D printed. Other parts are printed to verify the print quality and printing properties as mentioned below.

- Ninjaflex is printed as the membrane with PLA to check the adhesion and print feasibility. This print provided a good adhesion and reliability with selected print settings.
- The casing material (PLA) is printed along with PI-ETPU or protopasta to check the print feasibility. From this protopasta is selected because it is found that it has better adhesion properties with PLA than PI-ETPU.
- Only the heaters are printed in a cylindrical shape of length 10 mm with protopasta to study the resistance of the 3-D printed part based on the change in layer thickness, radius and infill percentage as shown in Table 4.2.
- Protopasta is 3D printed with an angle of 45 deg from the base to check design feasibility in case the design needs to have any angled heaters.

Based on these observations, various design choices and material choices are made for the actuator, which are used to experiment using test designs. The 3D printing settings for PLA, protopasta and Ninjaflex are presented in Table 4.1.

Print Setting Type	**PLA**	**Protopasta**	**Ninjaflex**
Printing Temperature (°C)	200	220	230
Heating Bed Temperature (°C)	50	50	50
Layer Thickness(mm)	0.2	0.2	0.2
Infill Percentage (%)	20	100	100
Extrusion Multiplier	1.2	1.2	1.4
Nozzle Diameter (mm)	0.4	0.4	0.4
Printing speed (mm/ min)	2000	2000	2000
Cam Dial	4	4	2
Outer Layers	3	3	3
Top and Bottom Layers	3	3	3

Table 4.1: 3D Printer Settings for PLA, Ninjaflex and protopasta

4.2 Heater test structures

Initially, the heater is designed as a block or cuboid as shown in Figure 3.4. The reason for this is the high surface area when compared to a cylindrical structural shape. So more fluid will be in contact with heater which can improve the rate of heat transfer. [46] However, to more closely relate to the analytical model of a sphere, and to have boundary conditions comparable with in the model in case of heat generation, the heater shape is changed to cylindrical. Furthermore,

S.No	Radius (mm)	Infill (%)	Layer thickness (mm)
1	2	20, 60 and 100	0.1, 0.15 and 0.2
2	3	20, 60 and 100	0.1, 0.15 and 0.2
3	4	20, 60 and 100	0.1, 0.15 and 0.2

Table 4.2: Heater resistance test parameters

to test the optimum print settings at which the resistance of the heater is lower (since the mode of power supply is voltage controlled), 27 different 3D prints are printed by changing the radius, infill percentage and layer thickness as shown in Table 4.2. Figure 4.1 shows the 3D printed heaters with conductive silver ink applied on the edges.

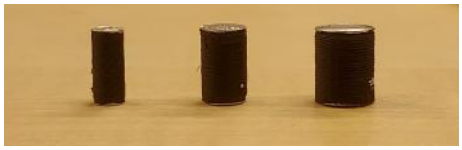

Figure 4.1: Heater 3D prints

From these test prints, it is confirmed that there is good adhesion between PLA and protopasta and also between PLA and Ninjaflex. Therefore, a feasible actuator design can be realised, using these selected materials and print settings. However, more tests needed to to be done on the total actuator design to test functional feasibility of the presented model.

4.3 Final Designs

4.3.1 First design

Since three different materials are required in the actuator design and the Flashforge can only print two, it is divided into two parts. The first part consists of a hollow cylinder that is designed with one open end and a membrane at the closed end. On the open end Ninjaflex is printed which acts as a gasket, to give good grip at the contact surface and prevent leakage of liquid. The material used for the cylinder is PLA and the material used for the flexible membrane is also Ninjaflex. The second part consists of a top, to enclose the cylinder, and a heater. The material used for the top is PLA and the heater is printed with Protopasta. Two screw holes of 3 mm in diameter, to hold the top and casing of cylinder together, are included. For the supply of power to the heater conductive silver is used. The Solidworks design of this model is shown in Figure 3.4. The 3D prints are made using the same designs; the first part is shown in Figure 4.2 and the second 3D printed part is shown in figure Figure 4.3.

Figure 4.2: 3D printed first part consisting of; Membrane: 3D printed with Ninjaflex (material in blue color) and casing: 3D printed with PLA (material in pink color)

Figure 4.3: 3D printed second part consisting of; Top: 3D printed with PLA (material in Pink color) and heater: 3D printed with Potopasta (material in black color)

4.3.2 Second design

The role of this design is to check the heat conduction within the actuator. Since the actuator design is closed, it is hard to study the heat flow within the actuator. To facilitate this an open top model as shown in Figure 3.5 is designed. In this design the heater is 3D printed using protopasta and the casing using PLA. Using this design the heat flow can be studied by using a thermal camera. Although this design does not closely represent the closed actuator due to the fluid surface being in contact with external surroundings, this is the closest approximation that can be done to study the heater and heat conduction and heat flow inside the actuator. The print settings used for this model are the same as shown in Table 4.1.

4.3.3 Third design

The third design as shown in Figure 3.6, has a similar structure as the second design, however, the effective dimensions are increased by a factor 2 as shown in figure Figure 3.5. The 3D printed part used the same materials and print settings as in the second design.

4.4 Holder

To perform the resistance measurement on the 3D printed heaters and to perform the test on the second and third designs a reliable setup is required. For this purpose 2 different holders are fabricated. The holder consists of Delrin top and bottom plates which are connected through the use of 6 mm screws and bolts. Alternatively any other non-conductive material that can withstand soldering can be used. Two bolts are used to adjust the height of the top plate relative to the bottom plate, therefore, the length of the screws used must be higher than the length of the heater. To provide power supply to the heater conductive copper tape strips are used to be in contact with heater. Wires are soldered to the copper strips through which the power supply is connected. Two different holders are fabricated; the first holder, shown in Figure 4.4, is used for resistance measurement and the second holder, shown in figure Figure 4.5, is used for heat flow measurement in the open top designs.

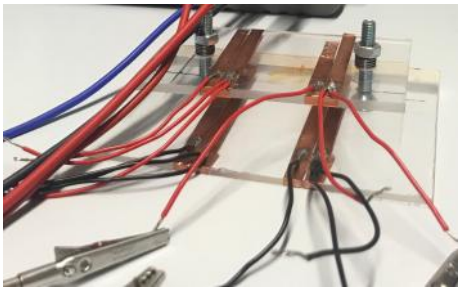

Figure 4.4: Setup for 4 point Resistance Measurement

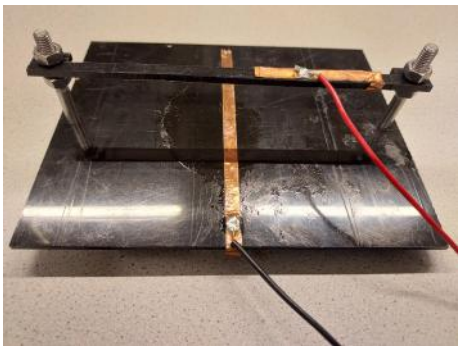

Figure 4.5: Holder for open top actuator clamping and power supply connections with copper tapes and soldered wires

4.5 Conclusion

The first design serves as an illustrative design to which the complete actuator can be designed. From this 3D printed model there are some changes which are required for designing a better actuator like the gasket and the flexible membrane. The gasket that is used did not prove to be as effective as it was thought to be, as there was still leakage when the actuator was filled with water. So a better water and oil tight design is required for the actuator. Furthermore, the flexible membrane properties need to be studied like load-deflection for optimum design of the membrane [47]. These studies are important to determine both the membrane deflection and the radius required to fit the shape of the tube as well as the thickness of the membrane needed to achieve this deflection. The second and third designs are simple designs to study the heat flow and heater properties for the used experimental setup to a limited extent, and it will be shown in Chapter 5 that they meet these requirement.

5 Measurements

In this chapter all the experiments that are done along with how the measurements are performed and their results are discussed.

5.1 Resistance measurements

As mentioned in Chapter 4, the heater designs are 3D printed with various parameters as shown in Table 4.2. The prints are made to measure the resistance of the heater with different print settings and to select the optimum heater design for the actuator. Even though the resistance of the 3D prints changes with each 3D print even when printed with the same print settings, the measured values give a good approximation on the typical range of the resistance.
The 4 point resistance measurement method is used to determine the resistance of the 3D printed heaters, since using this method allows to exclude the lead and contact resistances and to provide accurate resistance values [48]. The circuit design for 4 point measurement is shown in Figure 5.1. The experimental setup for the 4 point measurement is shown in Figure 5.2. In this setup, two copper strips are stuck side by side with a small spacing between each other (so that they are not in contact) on both the top and bottom plates. The 3D printed heaters (shown in Figure 4.1) are placed in between the top and bottom plates such that the heater edges are in contact with both copper strips on each plate. A wire is soldered to each copper strip, to provide contact with a digital multimeter. A Keysight 34461A model digital multimeter that has an inbuilt 4 point measurement option is used for measuring the resistance [49, P. 13]. The resistance measurement is done for every 3D printed heater and values are noted manually. Furthermore, the top and bottom parts of all the heaters used in the measurement are coated with conductive silver.

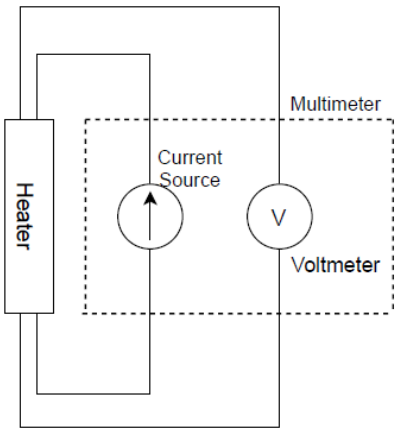

Figure 5.1: Circuit for 4 point resistance measurement.

5.2 Experimental Setup and Measurements

After fabrication, the experiments are conducted on the open top actuators shown in Figure 3.5 (named as V1 for reference) and Figure 3.6 (named as V2 for reference). These experiments are performed to analyse the heat conduction in the actuator and to determine the heater properties and their limits (since the standard data available on the protopasta is limited [42]). To perform these experiments the open top actuator is filled with olive oil and placed on the holder shown in Figure 4.5. The holder base as used in 4 point resistance measurement, has copper tape on the top and the bottom plate and a wire is soldered to each plate over the copper tape. The open top actuator model is placed on the holder base such that the heater ends that are

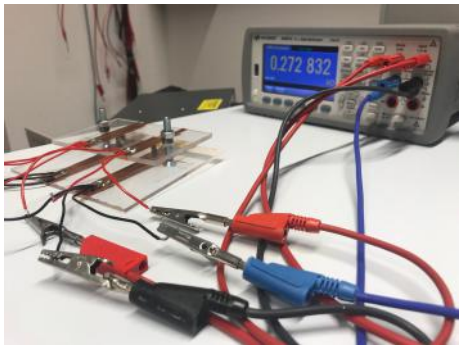

Figure 5.2: 4 point resistance measurement with connections to digital multimeter.

coated with conductive silver are in contact with the copper tape on the plates.
After the actuator is placed on the holder, the soldered wires are connected to the DC power supply. A thermocouple which is in connection with a digital multimeter is placed in the actuator such that it is in contact with the heater and immersed in olive oil. Since the holder top plate covers the heater the thermocouple can be used to get the temperature measurements in near proximity to the heater. Finally, a thermal camera that is connected to an iPhone is placed directly above the actuator using a stand and a phone holder such that it covers the actuator as a whole, as shown in Figure 5.3. This completes the experimental setup as shown in Figure 5.4. The experiments are performed for two open top actuators V1 and V2 with three different constant power values of 0.5 W, 0.7 W and 0.9 W. Since using current control could result in thermal runaway[1], a voltage source is used for ease of control. An Agilent E3631A 50 V programmable DC power supply is used with the MATLAB script to voltage control the power supply and log the voltage and current readings with time. The maximum power that can be supplied using this power supply is 0.9 W. The experiment is done for a total time of 600 s. In the first 10 s there is no power applied, which indicates the initial condition of the actuator. Then the constant power supply is started and maintained till the 310 s mark, which indicates the heating period and then from 310 s onwards the power supply is turned off till 600 s, which indicates the cooling down period. Important additional measurements that are taken during the time period of 600 s are the voltage readings from the thermocouple and the recorded video from the thermal camera. These measurements and how they are processed are discussed in later sections of this chapter.

5.3 Thermocouple measurements

The thermocouple is one of the most commonly used electrical devices for temperature measurement [50]. To measure the thermal distribution in the actuator, the open top actuator presented in Figure 3.5 and Figure 3.6 is used for testing. To get the temperature reading inside the actuator a thermal camera and a thermocouple are used. Though the thermocouple can only read a single temperature at the point of placement it can be used in conjunction with thermal camera readings, providing a reference temperature due to its reliability and accuracy. From the setup shown in Figure 4.5, it can be seen that the top plate covers the heater, this made thermal camera measurements at the heater not possible. Therefore, to study the heat generation with time near the heater, a thermocouple is placed in contact with the heater while making sure the tip of the thermocouple is within the oil. This thermocouple is connected to a multimeter to log the voltage values. The thermocouple measurements performed on 'v1' design at 0.5 W and 0.7 W cannot be considered due to the significant noise in measurement data because of wrongly placed thermocouple plugs.

[1] thermal runaway occurs when the increase in temperature acts as a positive feedback to further increase the temperature

The voltage readings from the thermocouple are logged using the digital multimeter for a given time. These voltage values are used to get the temperature readings. However, a thermocouple measures the values with respect to the reference voltage at the cold(reference) junction. The voltage values found in the literature, that can be used to relate the measured voltage to, are measured at temperatures of the cold junction at 0 °C [51]. However, in the experiment conducted the reference junction cannot be made 0 °C, so it is assumed to be at room temperature. Since the cold junction of the thermocouple is not at 0 °C, 'cold junction compensation' is required which is done using the table presented in [51]. Therefore, the conversion calculation of voltage to temperature is done as mentioned in [52]. The interpolation formula used for this is presented in Equation 5.1.

$$T_{\text{calc}} = ((T_{\text{max}} - T_{\text{min}}) * (V - V_{\text{min}})/(V_{\text{max}} - V_{\text{min}})) + T_{\text{min}} \tag{5.1}$$

Where

- T_{calc} is the temperature calculated for a given voltage.
- V is the voltage at which temperature T_{calc} is calculated.
- V_{max} is the maximum voltage measured from the thermocouple measurements.
- V_{min} is the minimum voltage measured from the the thermocouple measurements.
- T_{max} is the maximum temperature calculated highest voltage (V_{max}) from measurements after cold junction compensation.
- T_{min} is the minimum temperature related to the lowest voltage (V_{min}) from measurements after cold junction compensation.

And the V_{max} and V_{min} are the maximum and minimum voltages obtained from the thermocouple measurements respectively. Since the voltages from the measurements are taken at room temperature, as mentioned before cold compensation is required to get better accuracy in the temperature measurements. After the cold compensation of the voltages V_{max} and V_{min}, the equivalent temperatures are obtained from the thermocouple reference chart in [51]. Furthermore, these temperatures are cross verified using the calculator in [53], which have a inbuilt function of cold compensation when reference junction temperature is given as input. Later, using the interpolation formula in Equation 5.1 the remaining logged voltages from thermocouple are converted to temperature and these temperatures plots are shown in Chapter 6. Furthermore, from the temperature vs time plots, the heating and cooling time constants are determined. To determine these time constants and further predict the behaviour of model an exponential curve fitting is applied to the plots. And the time constant during heating TC_{heat} and time constant during cooling TC_{cool} are mention in Chapter 6.

5.4 Thermal camera measurement

Using the thermocouple, the temperature at a particular point can be obtained. However, to study the temperature distribution in the whole model there is a need for a different type of measurement. For this purpose, the "Flir One Pro" thermal camera [54] is used. The FLIR thermal camera is connected to an iPhone, then through the use of the Flir One application available for mobiles the thermal images are captured. Furthermore, a video can be recorded which shows the temperature distribution in the design over the required time period. The thermal camera shows the temperature value in a particular location using a color coding.

The FLIR software available for processing thermal images from the Flir camera is only suitable for images. But to study the temperature distribution in the model with time, a video is required. Therefore, to process and analyse the whole video, MATLAB image processing is used.

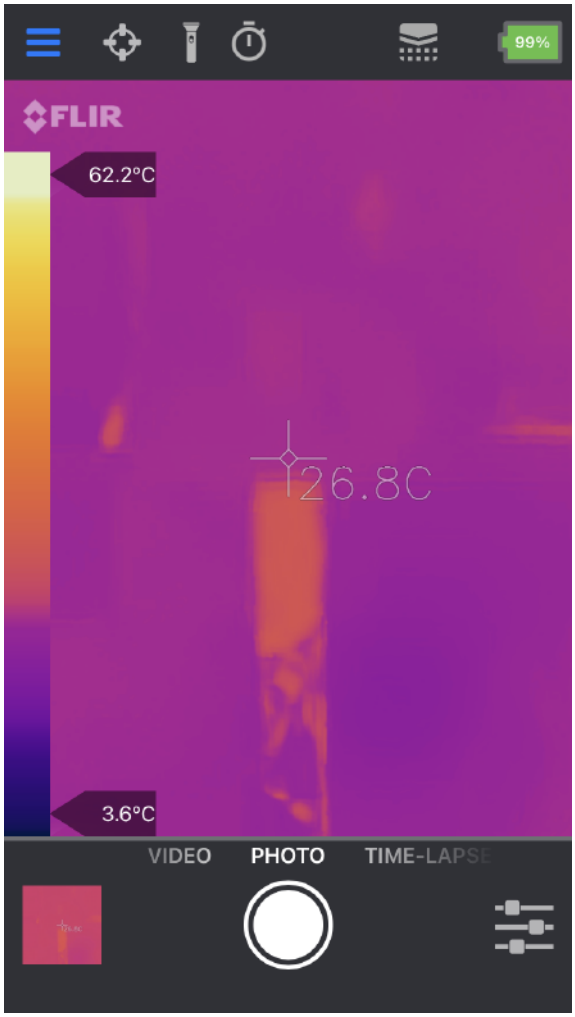

Figure 5.3: Screenshot of locked IR scale

The video from the Flir camera is processed frame by frame in MATLAB. However, when using the video feature in the thermal camera the recorded videos don't have a color bar (IR scale) that gives the relation between the temperature and the color coding of the thermal image. And even if the option of IR scale can be seen during the video it cannot be recorded and generally the color bar auto-adjusts with changes in time and temperature limits. Therefore, before starting the video the IR scale (color map bar) of the thermal image is calibrated. Initially, only the maximum limit of IR scale is matched using a soldering iron. Later on to achieve better resolution, ice is used to calibrate the minimum temperature in the IR scale. After this the IR scale is locked for the duration of the video. The temperature of the soldering iron is fixed at 60 °C and used to calibrate the max temperature of the IR scale and the ice is used to calibrate the minimum temperature of the IR scale. After that IR scale is locked, the solder iron and ice are removed from the frame, then a screenshot is taken as shown in the Figure 5.3, from which the IR scale is cropped and later used in processing the thermal video frames to map color to temperatures. It can be seen from Figure 5.3, that the minimum and maximum values of the IR scale does not perfectly match the set temperatures of ice and solder iron respectively, this can be due to emissivity of different materials [55] and also due to noise as the process is done in open surroundings and also the solder iron temperature could have an error. The IR scale calibration with ice to set minimum limit was not done for the video recorded at 0.5 W and 0.7 W powers for V1 model.
When processing the thermal image video, by utilizing the knowledge of the frame rate and

total number of frames obtained from the information of the video file, the frames at regular intervals of time can be calculated and processed. The image in every selected frame is also converted into a gray scale image using the limits of the color bar, where the intensity values in each pixel lies between 0 and 1. From these intensity values the temperature values are obtained. However, due to the noise in these thermal images there will be errors in the temperature values at each and every pixel. To reduce this noise the thermal image is further processed using an averaging filter. This usage of averaging filter gives more consistent results than the raw thermal image from the video, at the cost of image resolution. By selecting a certain pixel in the image and plotting its (averaged) temperature with time, the temporal change of temperature can be studied. Furthermore, by selecting the pixel values in a series such that they are in a straight line from (near the) centre of the heater to the edge of the actuator, the temperature along the radial direction of the actuator can be obtained.

Figure 5.4: Experimental Setup consisting of; test structure filled with olive oil place on the holder, thermal camera connected to an iphone, thermocouple connected to digital multimeter, DC power supply connected to soldered wires on holder, solder iron used for calibration IR scale of thermal camera.

5.5 Conclusion

Based on the resistance determined from the 4 point resistance measurements and the design requirements, the heater parameters infill, layer thickness, and radius, are chosen of the test heaters. These observations were used to provide design parameters for the fabrication of the open top actuators. Since the voltage control is being used, to have high heat generation the lowest possible resistance is desirable. After selecting the heater parameters, these are used in 3D printing of the open top actuators used in the experiments. During the experiment, the voltage controlled constant DC power supply of 0.5 W, 0.7 W and 0.9 W are used. MATLAB code is used to control the DC power source to provide the constant power supply and readings of voltage and current are logged which can be used in resistance calculation of the heater. Using the same MATLAB code and a digital multimeter the voltage of a K-type thermocouple, which is placed in the open actuator, are logged. Thermal image video is recorded using a FLIR One Pro

thermal camera. These readings are used in further analysis to determine the time constant of the experimental structure, the results of which will be discussed in Chapter 6. By using varying values for the supplied power the temperature scaling with respect to change in power can be observed. Furthermore, since the tests are performed with open top actuators (V1 and V2, where V2 is V1 scaled by a factor of two) the effect of time constant with change in radius and length can obtained. Finally the thermal images can be used to observe the temperature distribution along the radius of the actuator.

6 Results

This chapter explains the results obtained from the measurements performed as mentioned in the Section 5.3 and the observations from these results.

6.1 Resistance measurements

As described in the section on resistance measurement, a '4 point measurement' is performed on all 3D printed heaters, as shown in the Table 4.2. The plots seen in Figure 6.1, Figure 6.2 and Figure 6.3 present the results of these measurements with three distinct radii. The graphs show that the heaters with a larger radius have less resistance, which is consistent with the formula for resistivity Equation A.2. Furthermore, the heater with a 0.2 mm layer thickness and 100 % infill has the lowest measured resistance, while the heater with a 2 mm radius, 0.15 mm layer thickness, and 20 % infill has the highest measured resistance. It is also apparent from the graphs that with the increase in infill percentage there is a decrease in resistance which is consistent with the results in [56, p. 4]. The increase in layer thickness has no apparent unambiguous effect as the resistance at 0.15 mm layer thickness is higher than the heaters with the same infill and radius at 0.1 mm and 0.2 mm layer thicknesses. This can be due to the various 3D print parameters and 3D print patterns however no definite reason can be deduced from these tests alone.

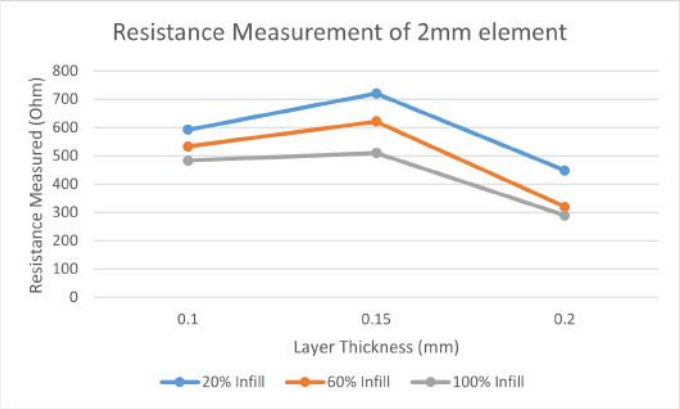

Figure 6.1: Resistance of 2 mm radius heaters measured using four point resistance measurement

Since the heaters with 100 % infill and 0.2 mm thickness have the lowest measured resistances these print parameters are used while printing the open top actuators shown in Figure 3.5 and Figure 3.6. Although the resistance of the heater decreases as the radius increases, other characteristics, such as the size of the actuator, its thermal time constant and available space, must be considered while selecting the heater's radius.

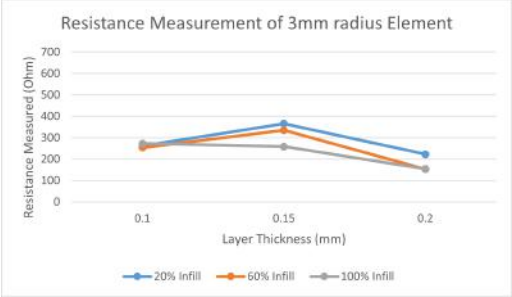

Figure 6.2: Resistance of 3 mm radius heaters measured using four point resistance measurement

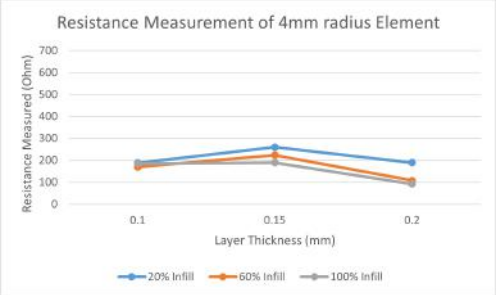

Figure 6.3: Resistance of 4 mm radius heaters measured using four point resistance measurement

6.2 Thermocouple measurements

As mentioned in the thermocouple measurement description in Section 5.3, the thermocouple was placed in the actuator such that it is in contact with the heater and immersed in oil. Using MATLAB and a digital multimeter the voltage readings of the thermocouple during the experiment are logged. Later cold junction compensation is implemented on the voltage readings from the thermocouple and then using the interpolation method, temperatures at each voltage are determined. Finally, temperature vs time graphs at different power supply levels for the design V2 are plotted. The graphs shown in Figure 6.4 display the temperature with time for the V2 model with the heater of radius 4 mm and height 26 mm when supplied with three different power supply levels.

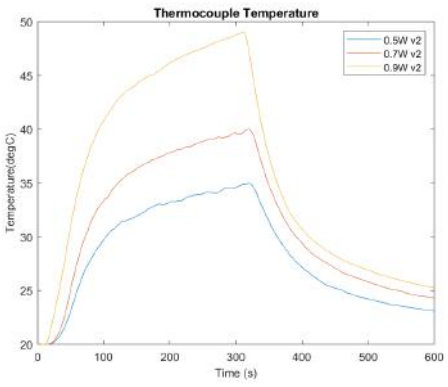

Figure 6.4: Thermocouple temperature plots for V2 model at power P =0.5 W,0.7 W,0.9 W

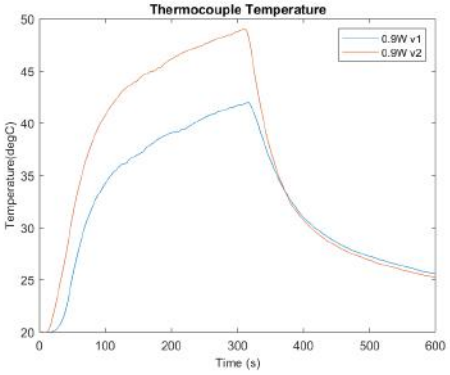

Figure 6.5: Thermocouple temperature plots for V1 and V2 models at P =0.9 W

Figure 6.5 shows the comparison of temperature plots at 0.9 W of models V1 and V2. From the graphs it can be seen that the first 10 s the temperature is uniform and after the 10 s mark there is a rise in temperature till 310 s, indicating the heating period. After 310 s there is a drop in temperature indicating the cool-down period. The model V1 reaches higher temperatures that V2 at same input power.

From the plots shown in Figure 6.5 and Figure 6.4 the thermal time constants are determined by fitting an exponential curve. The time constants are determined for the heating period and cooling period separately for model V2 at different supplied powers and these are presented in Figure 6.6. Moreover for the comparison of the time constants between V1 and V2 at 0.9 W supplied power, the plots shown in Figure 6.7 are presented and studied. Tc in these figures represents the time constant(τ) of the obtained curve fit. The maximum measured temperature $T_{\max}$, heating time constant τ_{heat} and cooling time constant τ_{cool} from the plotted graphs are presented in the Table 6.1.

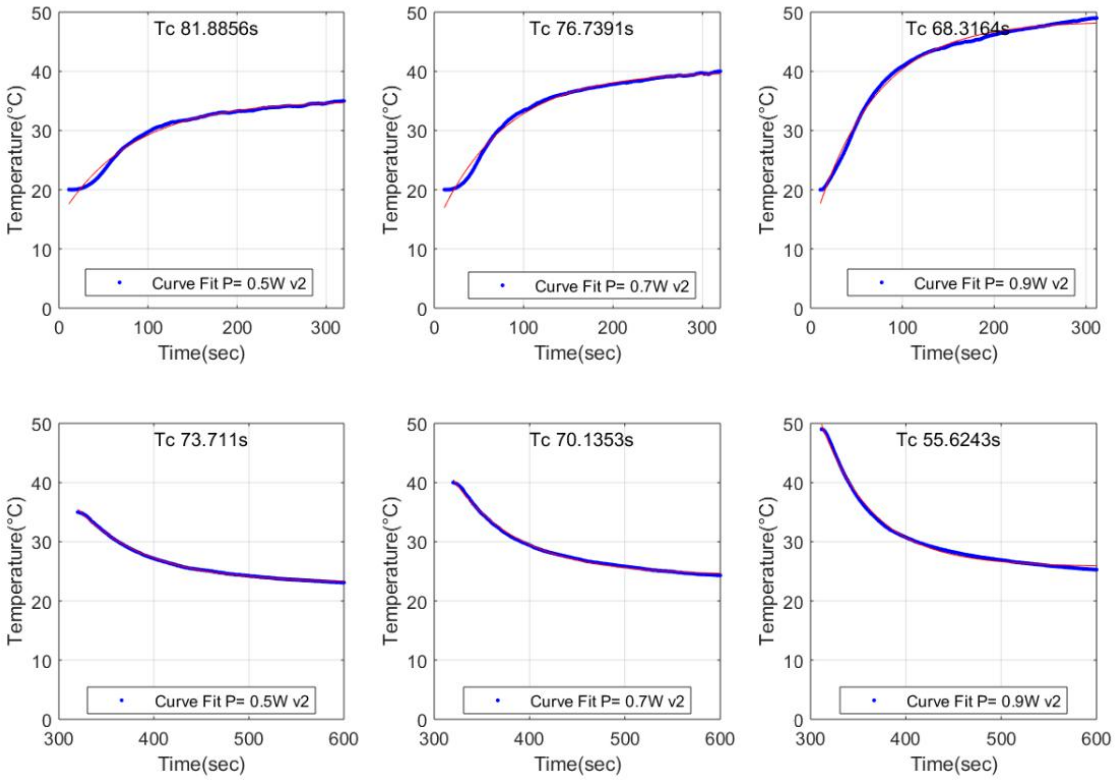

Figure 6.6: Thermocouple temperature plots (blue) with exponential fits (in red) for model V2 . The 'Tc' values are the time-constants as determined from the fits. Top: for heating. Bottom: for cooling. Left: P =0.5 W. Middle: P =0.7 W. Right: P =0.9 W

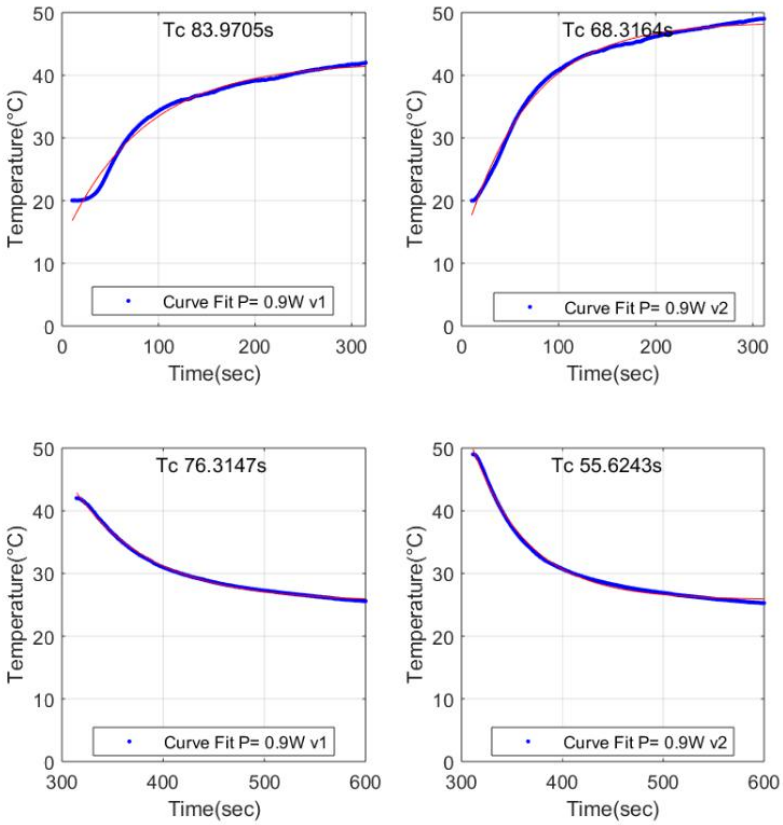

Figure 6.7: Thermocouple temperature plots (blue) with exponential fits (in red). The 'Tc' values are the time-constants as determined from the fits. Left: Design V1. Right: Design V2. Top: Heating. Bottom: Cooling. P =0.9 W for all cases

6.3 Thermal camera measurement

Due to the limitation of the actuator holder covering the heater, it is not possible to perform thermal image analysis on the heater itself. Therefore a point (pixel) near to the heater and which is not covered by the holder is selected from the image. The temperatures at the selected point with change over time at various supplied powers are plotted as shown in Figure 6.8 for both V1 and V2 test structures. These graphs are further used in calculation of the time constants during the heating and cooling phases of the experiments.

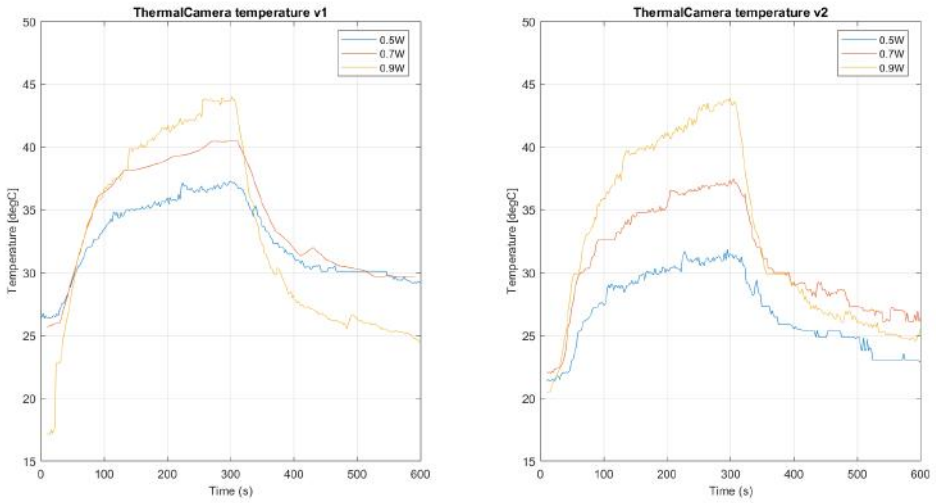

Figure 6.8: IR camera temperature vs time plots for V1 model (on left side) and V2 model (on right side), at powers P =0.5 W,0.7 W and 0.9 W

The time constants calculated for test structures V1 and V2 at various supplied powers are presented in Figure 6.9 and Figure 6.10 respectively. The maximum temperature measured $T_{\max}$, heating time constant τ_{heat} and cooling time constant τ_{cool} from the plotted graphs are presented in the Table 6.1. By using the IR camera it is possible to study the temporal temperature distribution along the radial direction (from the heater at the centre towards the edge). The temperature distribution plots are shown inFigure 6.12 and Figure 6.13.

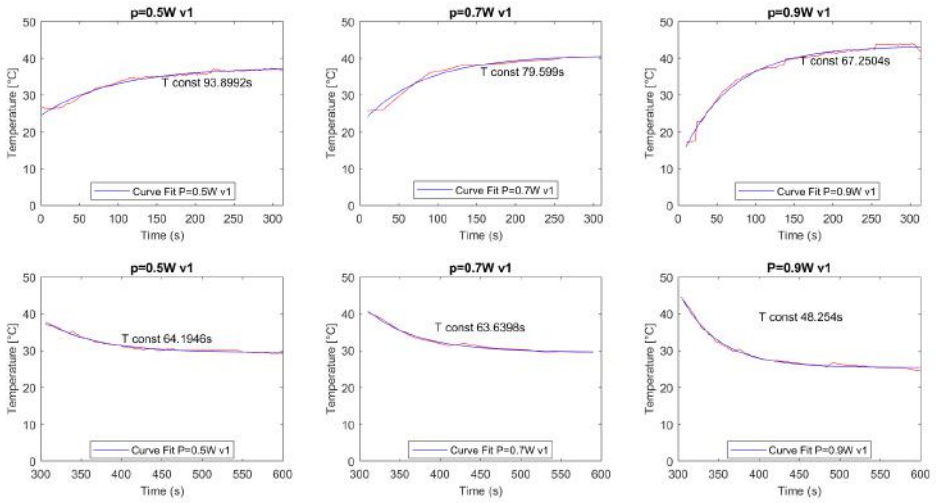

Figure 6.9: IR camera temperature plots (red) with exponential fits (in blue) for design V1 . The 'T const' values are the time-constants as determined from the fits. Top: for heating. Bottom: for cooling. Left: P =0.5 W. Middle: P =0.7 W. Right: P =0.9 W

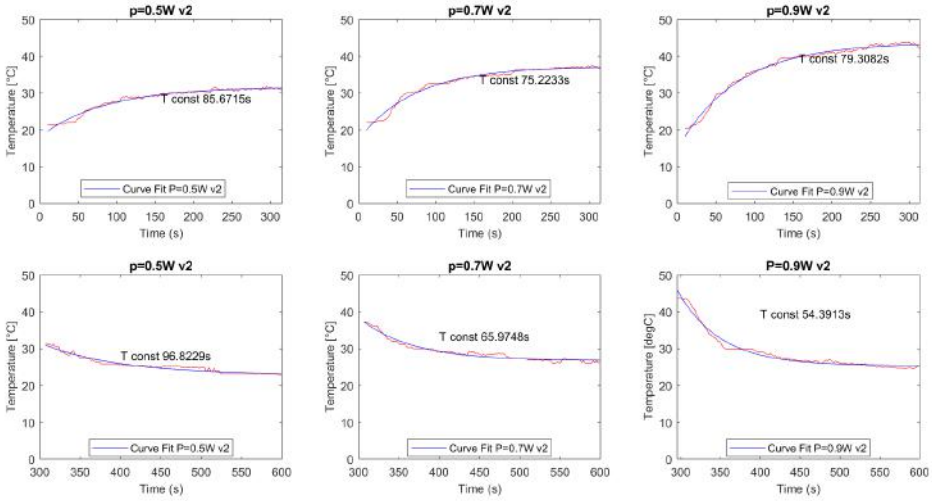

Figure 6.10: IR camera temperature plots plots (red) with exponential fits (in blue) for design V1 . The 'T const' values are the time-constants as determined from the fits. Top: for heating. Bottom: for cooling. Left: P =0.5 W. Middle: P =0.7 W. Right: P =0.9 W

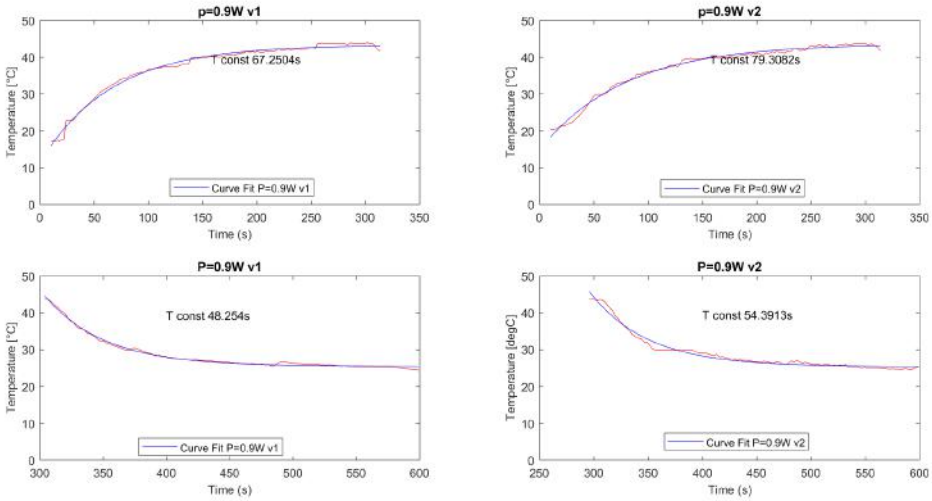

Figure 6.11: IR camera temperature plots plots (red) with exponential fits (in blue) for design V1 on left and design V2 on right. The 'T const' values are the time-constants as determined from the fits. Top: for heating. Bottom: for cooling. All plots at P =0.9 W

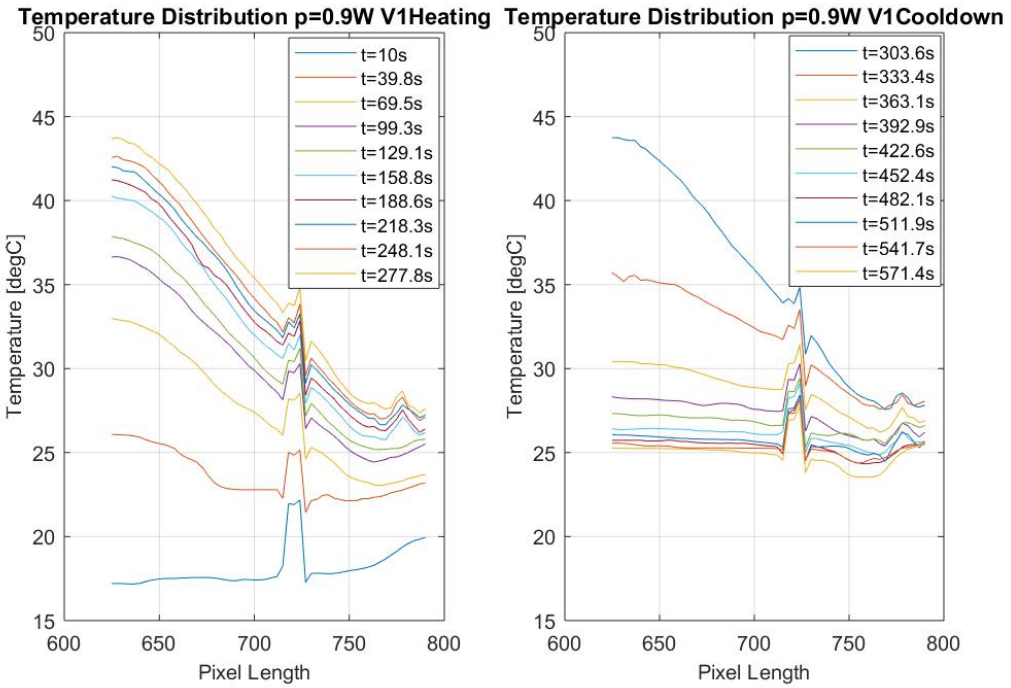

Figure 6.12: IR camera temperature distribution along the radius of the V1 model at p =0.9 W. Left side: Heating, Right side: Cooling down

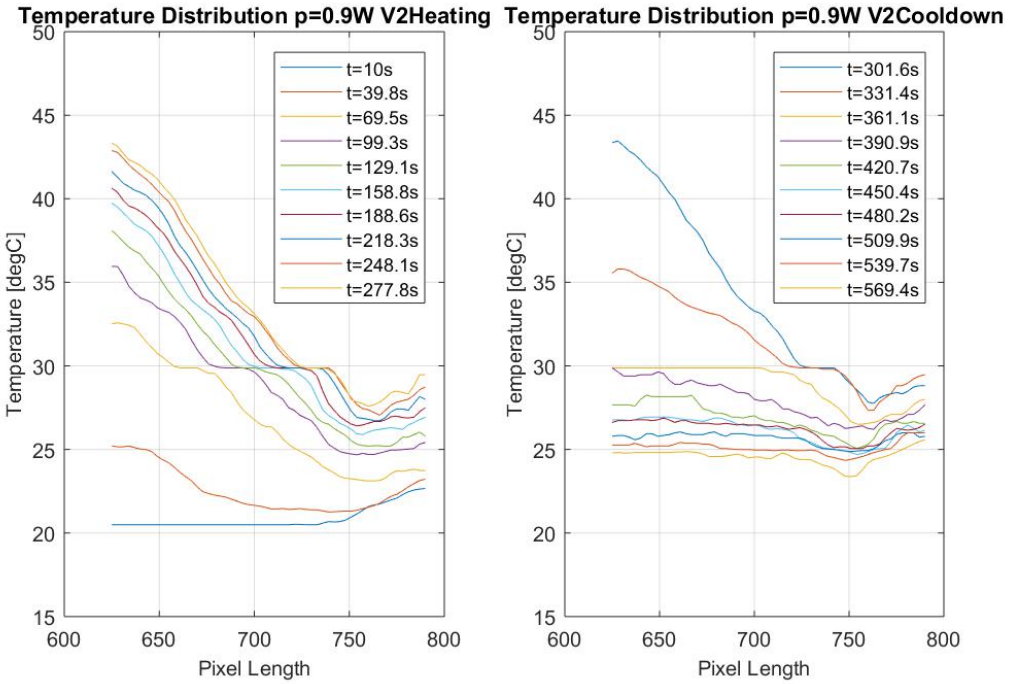

Figure 6.13: IR camera temperature distribution along the radius of the V2 model at p =0.9 W. Left side: Heating, Right side: Cooling down

Model	Power	Thermocouple			Thermal Camera		
	(W)	T_{max} (°C)	τ_{heat} (s)	τ_{cool} (s)	T_{max} (°C)	τ_{heat} (s)	τ_{cool} (s)
V1	0.5	-	-	-	37.29	93.89	64.19
V1	0.7	-	-	-	40.53	79.59	63.63
V1	0.9	42	83.97	76.31	44.014	67.25	48.25
V2	0.5	35	81.88	73.71	31.8	85.67	96.82
V2	0.7	40	76.73	70.13	37.43	75.22	65.97
V2	0.9	49	68.31	55.62	43.9	79.30	54.39

Table 6.1: Time Constant and Maximum Temperature Results

6.4 Discussion

The temperature graphs of the structures V1 and V2 from the thermocouple and the IR thermal camera are presented in this section. From the temperature graphs in Figure 6.4 and Figure 6.8 it can be clearly interpreted that with increase in power there is an increase in maximum temperature, as expected. This is supported by the analytical solution represented in Equation 2.86, Equation 2.88 and Equation 2.74, since with increase in power, the heat generation(g_o) is expected to increase which effects the $\Phi(r)$ term. Moreover, the maximum temperatures (T_{max}) reached in structure V1 are higher than V2 according to the plots obtained from the IR camera shown in Figure 6.8 and presented in Table 6.1. Which means that when equivalent power is supplied to V1 and V2, V1 has more heat generation than V2. However, the thermocouple readings in case of V1 at 0.9 W show otherwise which can be clearly seen in Figure 6.7. One possibility can be the poor placement of the thermocouple, further verification of this result with thermocouple measurements at 0.5 W and 0.7 W is not done since the thermocouple data at those powers was incorrect. Since the other readings from the IR camera analysis show a better consistency the readings from thermocouple of V1 structure at 0.9 W is neglected for comparison.

The thermal time constants are determined from the processes of heating and cooling of the test structures and these are presented in the figures 6.6, 6.9 and 6.10. From these graphs it is observed that the time constants of both heating and cooling of the structure decreases with increased power input. Except for an anomaly at 0.9 W in the V2 structure in the IR camera measurements, where the heating time constant is higher than the heating time constant at 0.7 W. Here, there is an error of 5.4 % in τ_{heat} at 0.9 W with respect to τ_{heat} at 0.7 W(in Figure 6.10), and one of the possibilities is an error in curve fitting due to not selecting close to optimal starting points for the curve, resulting in a local optimum being found instead of a global optimum. Therefore, the thermocouple measurements for V2 in Figure 6.6 looks more persuasive in this specific case. Furthermore, the time constant for cooling (τ_{cool}) is decreasing when a structure was provided with higher power. This behaviour is consistent with thermocouple measurements shown in Figure 6.6. Since there is no effect of power during cool down, the decrease in time constant can be related to the change in convection heat coefficient at higher temperatures.

From the graphs presented in Figure 6.8 it is observed that the calibration of both the lower and higher limits of the IR scale is providing better results as the graphs in V2 have better resolution than V1. Since the IR scale calibration of the minimum temperature is not performed on the V1 structure, the minimum temperature shown in the graph 6.8, is the result of the automatically set minimum temperature of the thermal camera. When the time constants during heating from the thermal camera readings are compared between V1 and V2 shown in Figure 6.9 and Figure 6.10 the τ_{heat} of V2 at 0.5 W and 0.7 W is lower when compared to the τ_{heat} of V1. However at 0.9 W the τ_{heat} of V1 is lower than τ_{heat} of V2. Henceforth the conclusions and discussions made in Chapter 7 are based on the results presented in this section and the simulations obtained from the analytical model in Chapter 2.

6.5 Conclusion

The results from the 4 point resistance measurement of the heater showed that, the heaters 3D printed with 0.2 mm layer thickness and 100 % infill gives lower resistance when compared with heaters of similar radius. Moreover, with decrease in radius the resistance increases as shown from graphs 6.1, 6.2 and 6.3. These results can help in selecting the heater, based to the design requirement. Base on this results the open top actuators designed in Figure 3.5 and Figure 3.6 with the print setting of 0.2 mm layer thickness and infill percentage of 100 % to attain lower resistance.
The heating tests are performed on the actuators (Figure 3.5 and 3.6) and the measurements are taken using thermocouple and thermal camera(IR camera). The temperatures plots obtained from these measurements are used to determined the time constants. The results from the measurements are further compared to the analytical equations and simulations from Chapter 2 discussed in Chapter 7.

7 Discussion and Conclusions

From the measurement results shown in Figure 6.6, Figure 6.9 and Figure 6.10 it can be seen that with increase in power there is a decrease in time constant, as stated in Section 2.5 the time constant is dependent on the term $\frac{1}{\alpha\lambda^2}$. One of the possibilities for this decrease in time constant with the increase in power can be that the average temperature is increased and with the increase in temperature there is a change in thermal conductivity and density [25] [38, P 351], which effect the thermal diffusivity (α). These dynamic changes can effect the time constant(τ_{heat}) to a certain extent. Furthermore, the λ_{n} is depends on the convection coefficient and thermal conductivity as shown in Equation 2.71 and Equation 2.82, which further effects the time constants. Moreover, the curve fits also have errors due to, e.g., selection of starting points. This can also be the reason for the decrease in cooling time constant (τ_{cool}) at different supplied powers for both V1 and V2 structures, shown in figures 6.6, 6.9 and 6.10. However, in Figure 6.10 at 0.9 W this consistency fails. So, more experiments are needed to determine the reason for this behaviour.

From the temperature graphs obtained for V2 using the thermocouple (Figure 6.5) and the IR camera (Figure 6.8), it can be seen that the maximum temperature obtained from the thermocouple reading is higher than the maximum temperature obtained from the thermal image. This can be due to the difference in the measurement points as the point considered for the thermal image analysis is farther away from the heater when compared to the thermocouple placed near the heater. Moreover, the emissivity of the oil could have affected the measurements of the IR camera [55]. The temperature distribution shown in Figure 6.12 and Figure 6.13 gives an approximation of the temperature gradient with change in radial position at a given time instance.

From the graphs obtained from analytical solutions shown in figures 2.6, 2.13 and 2.20 the time constant (τ) during cooling and heating decreases with a decrease in radius. This can also be supported from the Figure 6.11. However, this is in opposition to the thermocouple measurements shown in Figure 6.7. Moreover the T_{max} in V2 is higher than T_{max} in V1 which is also inconsistent with the IR camera readings and therefore it is assumed that there is an error in thermocouple measurements due to improper placement. So a more robust placement of the thermocouple is required for better readings and more measurements to support this. When the time constants during heating from the thermal camera readings are compared between the V1 and the V2 structures, as shown in Figure 6.9 and Figure 6.10, the τ_{heat} of V2 at 0.5 W and 0.7 W is lower when compared to the τ_{heat} of V1, however at 0.9 W the τ_{heat} of V1 is lower than τ_{heat} of V2. This can be due to use of non-calibrated IR scale at minimum temperature value, during the measurements with P =0.5 W and 0.7 W.

It is also important that in the V1 and V2 models, there is a scale in length of the heater along with the radius. The effect due to the change in length is ambiguous as the analytical equations that are solved in Chapter 2 are limited to a 1D sphere. Due to the complexity of solving the analytical equations in cylindrical coordinates and time constraints these could not be implemented in this assignment but solving the analytical equations for a cylinder would provide better approximations to the behaviour of the actuator in terms of time constant and design parameter approximation, as the experimental model is close to a cylinder rather than that of a sphere and includes the height in the equations [20, P. 148].

During the experiments with the open top actuators shown in Figure 3.5 and 3.6, the measurements are performed in open surroundings. As the open surroundings are dynamically changing there might be some undetermined effects in the measurements which cannot be predicted. Therefore, a better controlled environment is preferred to perform experiments. Moreover, the experimental model is open top to observe the temperature distribution, but in the actual application the actuator will be closed. This will also affect the parameters like the convection coefficient (h), affecting the time constant as well. Furthermore, a better IR camera can be used for the image analysis. For example, an IR camera which can show an IR scale during recording and maintain a good resolution of IR scale to map the relation from temperature to color (or even better; store temperature values directly).

Even though a complete design of an actuator is not presented in this project due to limited availability of the 3D printer(s), an approximate study on the design parameters can be done theoretically. For this theoretical calculation, the lowest time constant heating τ_{heat} =68 s is assumed from the results presented in Table 6.1 along with the parameters shown in Table 7.1. Thereafter, using the formula for the time constant presented in [57] [58], which can be used to calculate the time and external temperature required to reach the set change in (relative)temperature by using the τ_{heat} from the measurements:

$$t = -\tau \ln\left(\frac{T - T_{\max}}{T_{\text{i}} - T_{\max}}\right) \tag{7.1}$$

where

- T is the required temperature to reach the set temperature difference (ΔT).
- $T_{\max}$ is the maximum temperature.
- T_{i} is the initial temperature.
- t is the time required to reach temperature T.
- τ is the time constant.

Parameter type	**Value**
Radius of the tube to be blocked	0.001 m
Required Volumetric change	4.19×10^{-9} m^3
Time constant for heating	68 s
Temperature difference Required, ΔT	20 °C
Initial Temperature	20 °C
Thermal expansion coeff.	7×10^{-4} °C^{-1}
Minimum radius of membrane	0.003 m
Radius of heater	0.002 m
Height of the heater	0.01 m

Table 7.1: Parameters used to determine time and actuator dimensions

Using this formula and the parameters from Table 7.1 the time t required to reach the temperature T is presented with respect to the maximum temperature $T_{\max}$ and shown in Figure 7.1. From this graph, it can be seen that the minimum $T_{\max}$ required to achieve a temperature difference($\Delta T = T - T_{\text{i}}$) to the initial temperature of 20 °C is 936.7 °C, represent by a marker in Figure 7.1. For a $T_{\max}$ higher than 936.7 °C a switching time less than 1.5 s can be attained. This can be further improved by using materials with better thermal diffusivity and decreasing the radius of the actuator as shown in Figure 2.20.

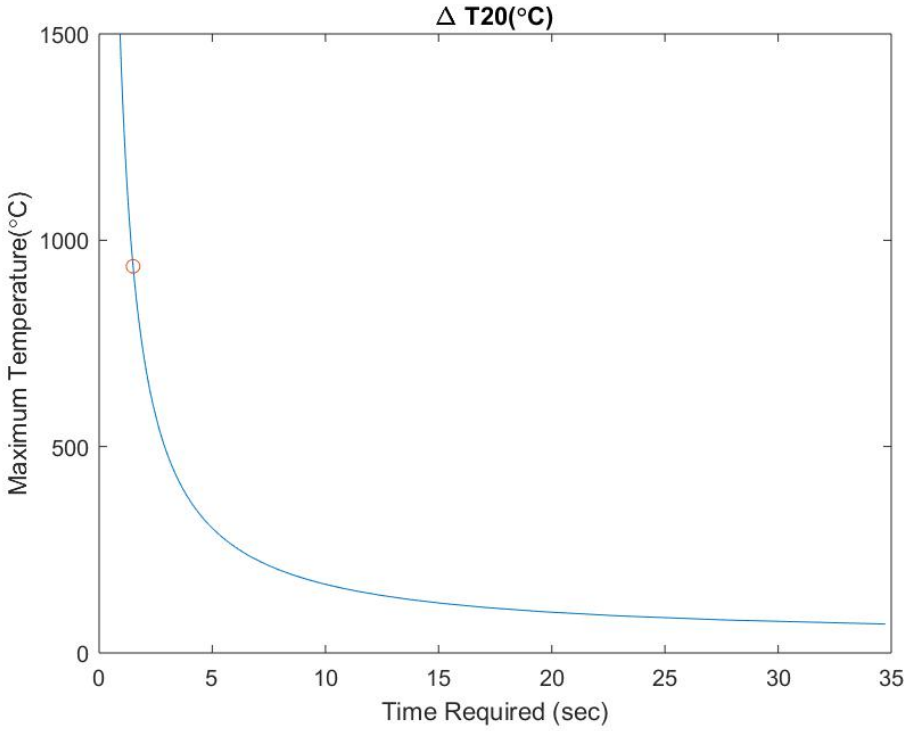

Figure 7.1: Time t required vs Maximum temperature $T_{\max}$ at a ΔT of 20 °C and τ 68 s

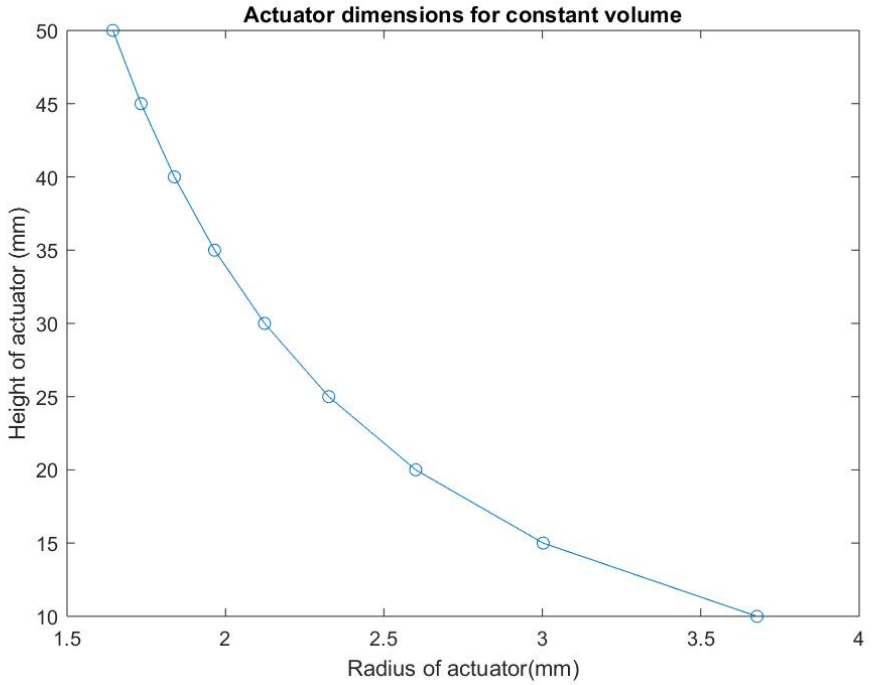

Figure 7.2: Internal radius and height of actuator for constant volume, this dimensions already include the volume of take a heater of radius 2 mm and height 10 mm

However, the attained dimensions only apply to heating where the speed at which the temperature increases can be controlled by increasing the power input to the actuator. But in case of quenching to realise a switching time of 1.5 s an additional cooling mechanism is required as

it is hard to attain it by natural cooling, as is supported from FEM simulation as shown in Figure 7.3. The actuator designed using these parameters might be useful in applications where the switching time required is lower.

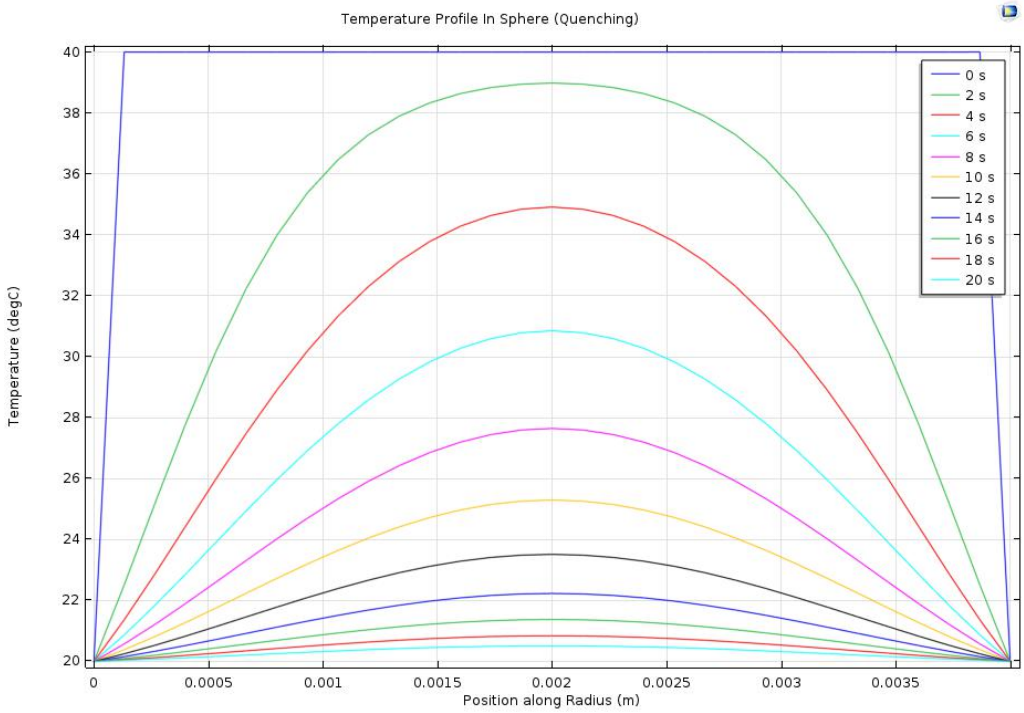

Figure 7.3: COMSOL Sphere temperature profile, cooling down from 40 °C to 20 °C and radius=2 mm

A Appendix 1

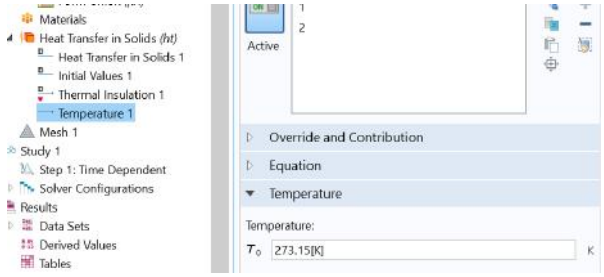

Figure A.1: COMSOL simulation of Transient analysis of slab, Boundary temperature

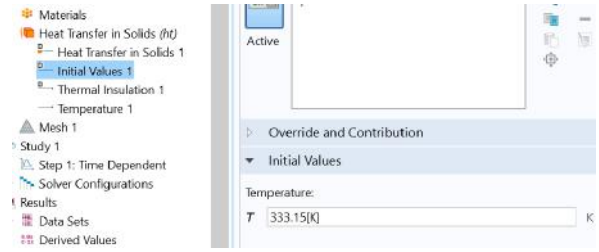

Figure A.2: COMSOL simulation of Transient analysis of slab, Initial temperature

$$dl = L_0 \alpha (t_1 - t_0) \tag{A.1}$$

Where

- dl = change in object length (m)
- L_0 = initial length of object (m)
- α = linear expansion coefficient ($\mathrm{m\,m^{-1}\,°C^{-1}}$)
- t_0 = initial temperature (°C)
- t_1 = final temperature (°C)

$$R = \rho \frac{L}{A} \tag{A.2}$$

- R is resistance (in ohm)
- L is length (in meters)
- A is area (in square meters)

Bibliography

[1] "Filament Properties Table." https://www.simplify3d.com/support/materials-guide/properties-table/.

[2] J. A. Lenssen, H. Naghibi, and M. Abayazid, "Evaluation of design aspects of modular pneumatic soft robotic endoscopes."

[3] H. I. Ali, S. Noor, S. Bashi, and M. Marhaban, "A review of pneumatic actuators (modeling and control)," *Australian Journal of Basic and Applied Sciences*, vol. 3, no. 2, pp. 440–454, 2009.

[4] E. E. Topçu, Yüksel, and Z. Kamış, "Development of electro-pneumatic fast switching valve and investigation of its characteristics," *Mechatronics*, vol. 16, no. 6, p. 365–378, 2006.

[5] J. Wang, J. Pu, and P. Moore, "A practical control strategy for servo-pneumatic actuator systems," *Control Engineering Practice*, vol. 7, no. 12, pp. 1483–1488, 1999.

[6] L. Fracczak, M. Nowak, and K. Koter, "Flexible push pneumatic actuator with high elongation," *Sensors and Actuators A: Physical*, vol. 321, p. 112578, 2021.

[7] H. D. Yang, B. T. Greczek, and A. T. Asbeck, "Modeling and analysis of a high-displacement pneumatic artificial muscle with integrated sensing," *Frontiers in Robotics and AI*, vol. 5, p. 136, 2019.

[8] K. Li, Z. Lv, K. Lu, and P. Yu, "Thermal-hydraulic modeling and simulation of the hydraulic system based on the electro-hydrostatic actuator," *Procedia Engineering*, vol. 80, p. 272–281, 2014.

[9] V. Konev, E. Polovnikov, O. Krut, S. Merdanov, and G. Zakirzakov, "Investigation and development of the thermal preparation system of the trailbuilder machinery hydraulic actuator," *IOP Conference Series: Materials Science and Engineering*, vol. 221, p. 012001, 2017.

[10] K. Suzumori, S. Iikura, and H. Tanaka, "Flexible microactuator for miniature robots," *[1991] Proceedings. IEEE Micro Electro Mechanical Systems*, pp. 204–209, 1991.

[11] F. Pol, D. Wonnink, M. Elwenspoek, and J. Fluitman, "A thermo-pneumatic actuation principle for a microminiature pump and other micromechanical devices," *Sensors and Actuators*, vol. 17, pp. 139–143, 1989.

[12] M. F. Rahmat, N. H. Sunar, S. N. Sy Salim, M. S. Zainal Abidin, A. A. Fauzi, and Z. H. Ismail, "Review on modeling and controller design in pneumatic actuator control system," *International Journal on Smart Sensing and Intelligent Systems*, vol. 4, no. 4, p. 630–661, 2011.

[13] K. Nakahara, K. Narumi, R. Niiyama, and Y. Kawahara, "Electric phase-change actuator with inkjet printed flexible circuit for printable and integrated robot prototyping," in *2017 IEEE International Conference on Robotics and Automation (ICRA)*, pp. 1856–1863, 2017.

[14] G. A., G. O., and B. K, "Thermal hydraulic actuator," *Journal of Mechanical Engineering NTUU*, 2013.

[15] D. Jaladi, E. Languri, K. Nawaz, and G. Cunningham, "Innovative thermal distillation method using solar heat localization,"

[16] D. Jaladi, E. Languri, and B. Piras, "Sustainable waste water treatment using solar energy by heat localization through porous media," 11 2019.

[17] Y. Cengel and T. M. Heat, *A practical approach*. New York, NY, USA: McGraw-Hill, 2003. https://catatanabimanyu.files.wordpress.com/2011/09/heat-transfer-cengel-solution-manual.pdf.

[18] T. Myint-U and L. Debnath, *Linear Partial Differential Equations for Scientists and Engineers*. Birkha¨user Boston, 2007. http://sharif.ir/ moosavi/Myint-U$_D ebnath - Linear_P artial_D ifferential_E quations_f or_S cientists_a nd_E ngineers.pdf$.

[19] M. J. Hancock, "The 1-D Heat Equation." https://www.math.ubc.ca/~feldman/m267/heatSln.pdf, 2006. MITopencourseware.

[20] D. W. Hahn and M. N. Özişik, *Separation of Variables in the Spherical Coordinate System*. JOHN WILEY SONS, INC., 2012.

[21] Q. Q. Shi, A. M. Tian, S. C. Bai, H. Hasegawa, A. W. Degeling, Z. Y. Pu, M. Dunlop, R. L. Guo, S. T. Yao, Q.-G. Zong, and et al., "Dimensionality, coordinate system and reference frame for analysis of in-situ space plasma and field data," *Space Science Reviews*, vol. 215, no. 4, 2019.

[22] U. Author, "1-D Thermal Diffusion Equation and Solutions." https://ocw.mit.edu/courses/materials-science-and-engineering/3-185-transport-phenomena-in-materials-engineering-fall-2003/study-materials/handout_htrans.pdf, 2003.

[23] Ernesto, "Transient Heat Conduction: Analytical Methods." https://www.coursehero.com/file/31048908/Transient1pdf/.

[24] D. W. Mackowski, *Conduction Heat Transfer*. Mechanical Engineering Department, Auburn University, 2011.

[25] T. Alpaslan, T. Ismail, and T. Sebnem, "Measurement of Thermal Conductivity of Edible Oils Using Transient Hot Wire Method," *International Journal of Food Properties*, vol. 21, pp. 741–747, 2009.

[26] "Introduction to Engineering heat Transfer." https://ocw.mit.edu/courses/aeronautics-and-astronautics/16-050-thermal-energy-fall-2002/lecture-notes/10_part3.pdf, 2003.

[27] K. A. Smith and C. K. Colton, "TRANSPORT PHENOMENA: HEAT MASS TRANSFER." http://web.mit.edu/10.302/www/Fall2001/PROBLEMSETS/ps2_solutions.pdf, 2001.

[28] "Linear temperature expansion - online calculator." https://www.engineeringtoolbox.com/linear-thermal-expansion-d_1379.html.

[29] "Pla technical data sheet." https://www.sd3d.com/wp-content/uploads/2017/06/MaterialTDS-PLA_01.pdf.

[30] "Overview of materials for acrylonitrile butadiene styrene (abs), molded." http://www.matweb.com/search/DataSheet.aspx?MatGUID=eb7a78f5948d481c9493a67f0d089646&ckck=1.

[31] K. Xie, Y. He, J. Cai, and W. Hu, "Thermal conductivity of nylon 46, nylon 66 and nylon 610 characterized by flash dsc measurement," *Thermochimica Acta*, vol. 683, p. 178445, 2020.

[32] "Specific heat of some common substances." https://www.engineeringtoolbox.com/specific-heat-capacity-d_391.html.

[33] "Silicon transformer oil." https://www.hotdiskinstruments.com/applications/thermal-conductivity-silicone-oil/.

[34] "Silicon ttransformer oil." https://www.substech.com/dokuwiki/doku.php?id=silicon_transformer_oil.

[35] D. Lv, J. X. Sun, and J. Li, "The research and analysis on the bean transformer oil," May 2012.

[36] "Novec 7000 engineering fluid." http://www.lib-em.com/upload/1530774819393637.pdf.

[37] "Volumetric thermal expansion coefficients." https://www.engineeringtoolbox.com/cubical-expansion-coefficients-d_1262.html.

[38] C. Peri, *The extra-virgin olive oil chain*. John Wiley and Sons, Ltd, 2014.

[39] "Pla vs. abs." https://www.3dhubs.com/knowledge-base/pla-vs-abs-whats-difference/.

[40] "Pla, abs and nylon." https://markforged.com/blog/pla-abs-nylon/.

[41] PalmigaInnovations, "Palmiga - pi-etpu 95-250 carbon black." https://www.creativetools.se/hardware/3d-printers-and-accessories/filaments/flexible-filaments/pi-etpu-95-250-carbon-black.

[42] "Electrically conductive pla." https://cdn.shopify.com/s/files/1/0717/9095/files/CDP1xxxx_SDS.pdf.

[43] "Ninjaflex." https://ninjatek.com/ninjaflex/.

[44] "Ninjaflex properties." https://ninjatek.com/wp-content/uploads/2019/10/NinjaFlex-TDS.pdf.

[45] "Creator pro- flasforge." https://www.flashforge.com/product-detail/4.

[46] "Rates of heat transfer." https://www.physicsclassroom.com/Class/thermalP/u18l1f.cfm.

[47] "Chapter 5 membrane deflection and maximum pressure load," in *Nano and Micro Engineered Membrane Technology* (C. van Rijn, ed.), vol. 10 of *Membrane Science and Technology*, pp. 111–131, Elsevier, 2004.

[48] I. Miccoli, F. Edler, H. Pfnür, and C. Tegenkamp, "The 100th anniversary of the four-point probe technique: the role of probe geometries in isotropic and anisotropic systems," *Journal of Physics: Condensed Matter*, vol. 27, no. 22, p. 223201, 2015.

[49] "Digital multimeters." https://www.keysight.com/us/en/assets/7018-03846/data-sheets/5991-1983.pdf.

[50] J. Wu, "A Basic Guide to Thermocouple Measurements." https://www.ti.com/lit/an/sbaa274/sbaa274.pdf, 2018.

[51] "Type k thermocouple." https://www.thermocoupleinfo.com/type-k-thermocouple.htm.

[52] "How to convert thermocouple milivolts to temperature." https://www.instrumentationtoolbox.com/2011/05/converting-thermocouple-milivolts-to.html.

[53] "Thermocouple voltage to temperature calculator." https://us.flukecal.com/Thermocouple-Temperature-Calculator.

[54] "Flir one pro." https://www.flir.eu/products/flir-one-pro/.

[55] "Infrared emissivity table." https://www.thermoworks.com/emissivity-table.

[56] G. N. Meloni and M. Bertotti, "3d printing scanning electron microscopy sample holders: A quick and cost effective alternative for custom holder fabrication," *PLOS ONE*, vol. 12, no. 7, 2017.

[57] A. Pourmovahed and D. R. Otis, "An experimental thermal time-constant correlation for hydraulic accumulators," Mar 1990.

[58] "Thermal time constant (iec 60539-1)." http://www.mmea.com/document/thermistor/thermistor06.html.